Source Localization

Jochen H. Kurz, Thomas Schumacher, Lindsay Linzer, Barbara Schechinger, and Christian U. Grosse

Abstract Quantitative methods in acoustic emission (AE) analysis require localization techniques to estimate the source coordinates of the AE events as accurately as possible. There are a number of different ways to localize AE sources in practice, i.e. to obtain the desired point estimate in one, two, or three dimensions. This chapter starts with approaches for automated onset detection since the travel time information is one of the most critical input parameters for most localization approaches. In general, most localization methods presented in this chapter have in common that the travel time information from source to receiver is used for localizing an AE source. Most of the methods of AE localization discussed here were developed in the framework of earthquake seismology and GPS techniques. Array-type approaches, which were designed especially for plate-like structures, are also discussed. Different techniques for one, two and three dimensional source localization are described. Approaches based on numerical inversions as well as grid search and array localization approaches are discussed. Further concepts developed or adapted for the AE localization problem presented in this chapter use, e.g., neural networks, probabilistic approaches, or direct algebraic methods from GPS technology. Localization accuracy is influenced by various factors. Therefore, how to determine localization errors and some measures to ensure high localization accuracy are also listed and discussed.

J. H. Kurz (✉)
DB Systemtechnik GmbH, Bahntechnikerring 74, 144774 Brandenburg-Kirchmöser, Germany
e-mail: jochen.kurz@deutschebahn.com

T. Schumacher
Civil and Environmental Engineering, Portland State University, 1930 SW 4th Avenue, Portland, OR 97201, USA

L. Linzer
SRK Consulting (South Africa) (Pty) Ltd, SRK House, 265 Oxford Road, Illovo 2196, South Africa

B. Schechinger
Gänsackerstrasse 22, CH - 5024 Küttigen, Switzerland

C. U. Grosse
Department of Materials Engineering, Technical University of Munich, München, Germany
e-mail: grosse@tum.de

C. U. Grosse et al. (eds.), *Acoustic Emission Testing*, Springer Tracts in Civil Engineering, https://doi.org/10.1007/978-3-030-67936-1_6

Keywords Source localization · Onset determination · Grid search · Array localization · Iterative localization · Inversion · Nonlinear · Probabilistic · Localization errors

1 Introduction

Quantitative methods in acoustic emission (AE) analysis require localization techniques to estimate the source coordinates of the AE events as accurately as possible. There are many different ways to localize AEs in practice to obtain the desired point estimate in one, two, or three dimensions. The most appropriate technique depends on the objective of the experiment, the required resolution and on the geometric shape.

The methods of AE localization presented in the following section were developed in the framework of earthquake seismology and GPS techniques. Further approaches designed especially for plate-like structures are also discussed. The principal of earthquake source localization can be applied directly to AE source localization with minor modifications. A detailed description of earthquake localization methods can be found in, for example, Bormann (2002), Aki and Richards (1980) or Shearer (1999). These are also the main references for this chapter. AE localization is applied to a variety of construction materials and even used in medical and electrotechnical applications. Examples of AE localization applications can be found in Grosse (1996), Zang et al. (1998), Ohtsu (1998), Köppel and Grosse (2000), Moriya et al. (2002), Finck et al. (2003), Sellers et al. (2003), Finck (2005), Schechinger (2005), Kurz (2005), Baxter et al. (2007), Schumacher et al. (2012), Kundu (2014), Kalafat and Sause (2015), Kurz (2015), and Gollob et al. (2017).

Source localization as well as global positioning in space is an inverse problem. Employing the arrival time differences of the elastic wave emitted by a source and recorded at each sensor, the source location can be estimated. AE source parameters consist of the origin time (e.g. initiation of a rupture) and the source position in Cartesian coordinates (x_0, y_0, z_0). The computed location represents the point in space and time where the fracture initiated, i.e. a point source is assumed. The first arrival time of the elastic wave at each sensor is the onset time of the compressional wave (P-wave). If the onset of the shear wave (S-wave) is detectable, this information can be used either in combination with or instead of the P-wave onset. However, the S-wave is often difficult to identify in AE signals from civil engineering materials. If the distance between source and receiver is only a few wavelengths, the onset of the S-wave is hidden in the coda of the P-wave. In addition, due to the relatively short source-sensor separation, near field effects can be present, i.e. P- and S-wave modes are not yet completely separated (Finck and Manthei 2004). Finally, since the particle motion of an S-wave is normal to the propagation direction, and that of a P-wave is parallel to the propagation direction, a P-wave sensor is not designed to detect S-waves (see also chapter "Signal-Based AE Analysis"). The onset times, the coordinates of each corresponding sensor and information regarding the velocities of the

compressional and shear wave (if the shear wave can be detected) are needed for any kind of localization (1-dimensional, 2-dimensional and 3-dimensional). Provided a homogeneous and isotropic material, the direct (or straight) raypath between source and sensor can be used for calculation of the source location. However, if a layered or even a heterogeneous and anisotropic material is considered, or in the presence of boundaries (e.g. air voids, cracks) with significant acoustic impedance differences, the effects of the material on wave propagation and the raypath must be taken into consideration in order to achieve an accurate localization. Most of the methods discussed in this chapter assume a homogeneous and isotropic material, an assumption that is generally valid for AE analysis of construction materials. However, some examples considering non-homogeneous and non-isotropic materials will also be shown, for example, applications on wood and complex-shaped and cracked concrete members.

The following section starts with a description of automatic signal onset detection methods, which are critical when dealing with large data sets.

Different AE source localization techniques are discussed subsequently, beginning with simple methods that provide a rough estimate of the source coordinates to more complex methods that consider multiple factors affecting the wave propagation process to achieve the highest possible accuracy.

2 Principal of Localization Procedures

2.1 Automatic Onset Detection

The determination of the onset time of a transient signal is an important task in many fields of science and engineering. Seismology and AE studies are related fields that use the phenomenon of stored elastic energy being released as elastic waves due to sudden fractures in a rigid body (Spies et al. 2004). A strong relation exists between localization techniques in both seismology and AE analysis because both fields place similar importance on determining accurate onset times.

Accurate onset time determination can be carried out manually by an operator or automatically by a picking algorithm and depends on the onset definition itself. Leonard (2000) describes the true onset time of a seismic phase as the moment in time when the first energy of a particular wave phase arrives at a sensor. However, this definition is applicable to elastic waves in nearly all media. The onset time is usually picked as the point where a difference between noise and actual signal can be observed, although an experienced analyst will often extrapolate slightly back into the noise (Leonard 2000). These are also the requirements to a reliable automatic picker.

With some modifications, the algorithms used in seismology can be applied to AE signals. Since the number of recorded AE signals can be up to several thousand during one test, it is clear that automatic onset determination is a necessity.

In this context, it is referred to the convention suggested by Allen (1982), pickers are algorithms used to estimate the onset time of a phase and detectors are algorithms used to detect a phase (phase refers to, e.g. longitudinal or transversal wave).

In seismology, a variety of automatic onset time picking approaches are used. Two general approaches can be distinguished. On the one hand, a global strategy can be used, where the entire recorded signal is scanned for the onset. On the other hand, an iterative strategy can be employed, where a particular region is preselected first, and from which the onset is then determined more accurately (Kurz et al. 2005). The main trends are summarized subsequently.

The simplest form of onset picking is to use an amplitude threshold exceedance picker. However, a fixed threshold approach is typically not applicable to signals with small amplitudes and/or signals with a low signal-to-noise ratio (SNR) (Trnkoczy 2002). A widespread approach that uses a dynamic threshold, is the so-called STA/LTA (STA: Short Term Average, LTA: Long Term Average) picker by Baer and Kradolfer (1987). The approach is not applied to the raw signal directly, but a characteristic function computed from the signal's envelope. Here, the STA measures the instantaneous amplitude of the signal and the LTA contains information about the current average seismic noise amplitude. The difference between STA and LTA function is further defined by multiplying the characteristic function with frequency dependent parameters. Earle and Shearer (1994) chose a similar approach using a different envelope function. Because signal and noise of AEs in concrete often lie in the same frequency range (approximately 20 kHz up to 300 kHz), the STA/LTA picker does not produce results with sufficient accuracy.

Joswig (1990) combined the STA/LTA picker with a sonogram analysis of the seismic signal. This approach was tested by Kurz (2006) on AEs from concrete and was found to produce acceptable results.

Dai and MacBeth (1995) used an artificial neural network (ANN) for automatic picking of local earthquake data. The network was trained on noise as well as P-wave segments. This method is also not applied to the raw signal directly, but to the modulus of a windowed segment of the signal. The output of the ANN consists of two values, i.e. the parameters of a function that accentuates the difference between the actual output and ideal noise.

Modeling the signal as an autoregressive process is another approach for onset time determination. A detailed description of theory and application for seismic signals can be found in Sleeman and van Eck (1999), Leonard (2000) and Zhang et al. (2003). Akaike (1974), as well as Kitagawa and Akaike (1978), showed that a time series can be divided into locally stationary segments, each of which can be modeled as an autoregressive process. To solve the seismological localization problem, a seismic signal including the onset and a first estimate of the onset time is needed. The intervals before and after the onset time are assumed to be two different stationary time series. For a fixed order autoregressive process, the point at which the Akaike Information Criterion (AIC) is minimized determines the separation point of the two time series (noise and signal) and therefore the onset point (Sleeman and van Eck 1999).

In the domain of AE analysis Kurz et al. (2005) applied the principle of the autoregressive AIC picker in an automatic onset detection procedure. The results of the autoregressive AIC picker were then compared to manual picks and to an auto picker based on the Hinkley criterion, which was developed for AE from concrete by Grosse and Reinhardt (1999). Details and applications describing these approaches and comparisons with other methods can be found in, e.g. Kurz et al. (2005) and Schechinger (2005). In the following, only a short summary will be given. Further investigations and improvements on automatic onset detection for AE signals were carried out by, e.g. Sedlak et al. (2013), Mhamdi (2015), and Gollob (2017).

Furthermore, the SNR is affected by the degree of damage of the tested specimen and therefore, by the deterioration process itself. Due to this dependency, the SNR of AEs is generally not constant over the course of an experiment. Therefore, a reliable automatic picker that can handle data of varying quality is needed.

An autoregressive AIC picker gives picks (where the term 'picks' refers to the determined onset times) of higher quality when the AIC is only applied to the portion of the signal that contains the onset (Zhang et al. 2003). Therefore, the onset is defined initially by using the complex wavelet transform or the Hilbert transform. Both transforms lead to an envelope of the signal. Herein, only the Hilbert transform is used in the picking process (Fig. 1).

The Hilbert transform envelope is used for an initial pick of the onset using a fixed threshold. Each envelope is squared and normed, so that a constant threshold value can be applied to all signals (Fig. 1). A window of several hundred samples, e.g. 400

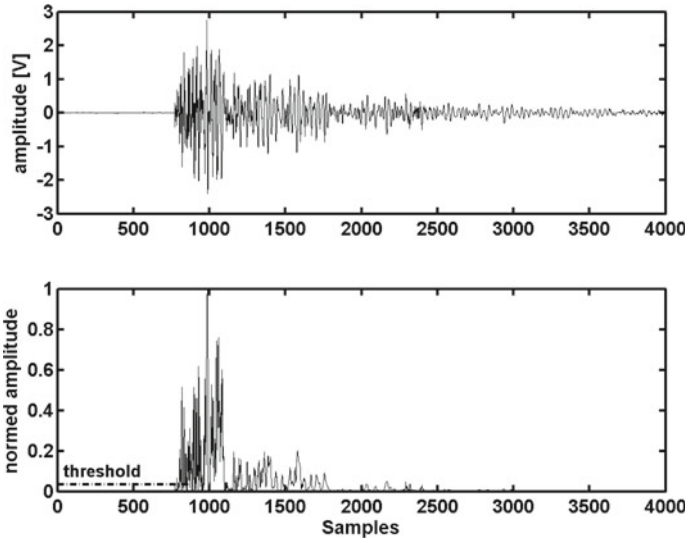

Fig. 1 Sample AE signal in the (top) time domain and (bottom) corresponding squared and normalized amplitude calculated with the Hilbert transform. A fixed threshold is drawn on the envelope for illustrative purposes

before and 150 after this point, is then extracted from the signal. Within this signal portion, the onset is determined using the AIC picker.

The advantage using an envelope calculated by the wavelet transform is that even for noisy signals the prearrangement of the onset by a threshold works consistently. The reason for this is that the envelope is calculated only for one scale, which has the most signal content, while most of the noise of is found in different scales.

However, if two or more signals of different amplitude and frequency superpose each other, i.e. if AEs occur in such a fast succession that more than one signal is recorded within the normal block length, the envelope calculated by the Hilbert transform should be used. In such a case, the wavelet transform can identify the wrong signal because of the automatic scaling.

The onset is determined by calculating the AIC function directly from the signal according to Maeda (1985):

$$AIC(t_w) = t_w \cdot \log\left(\mathrm{var}\left(R_w\left(t_{w,1}\right)\right)\right) + (T_w - t_w - 1) \cdot \log(\mathrm{var}(R_w(1 + t_w, T_w))) \quad (1)$$

The index w from the time series R_w indicates that not the whole time series is taken, but only the chosen window containing the onset (described above). T_w is the last sample of the curtate time series, t_w ranges through all samples of R_w and *var* denotes the variance function. The term R_w (t_w, 1) means that the variance function is only calculated from the current value of t_w while R_w (1+ t_w, T_w) indicates that all samples ranging from 1 + t_w to T_w are taken. The sample variance *var* or σ^2_{N-1} is defined as (Kreyszig 1993):

$$\sigma^2_{N-1} = \frac{1}{1-N} \sum_{i=1}^{N} (R_i - \Gamma)^2 \quad (2)$$

where N denotes the length of the signal, R_i is sample, i of the time series, R and Γ is the mean value of the whole time series, R.

In the ideal case, the global minimum of the AIC function corresponds to the onset point of the signal (Fig. 2).

A comparison of the AIC-picker with the Hinkley picker shows that the AIC-picker produces more accurate results (Fig. 3). The value of the deviation (in percentage) between the localization using manual picks and the localization using the AIC-picker greater than 5 mm is 11%. The Hinkley-picker produces a deviation of up to 68% compared to the manual picks. The number of well-localized events using the Hinkley-picker can be sufficient to visualize the general shape of the fracture process. How-ever, this might not be valuable for all cases and a higher rate of correct picks is recommended.

Taking into consideration that manual onset determination is also subject to various errors, it was shown that the AIC-picker produces sufficiently reliable results for AE source localizations. Therefore, the AIC-picker, or at least an iterative strategy,

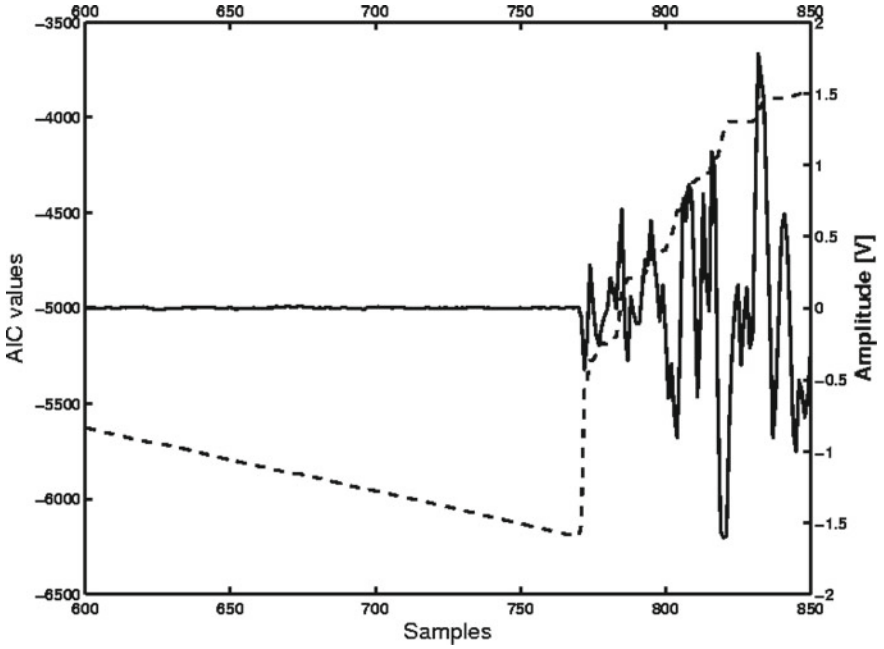

Fig. 2 The AIC is used for onset determination only for the selected part of the signal containing the onset, which is displayed by the solid line. The minimum of the AIC function, which is represented by the dashed line, denotes the onset time of the signal

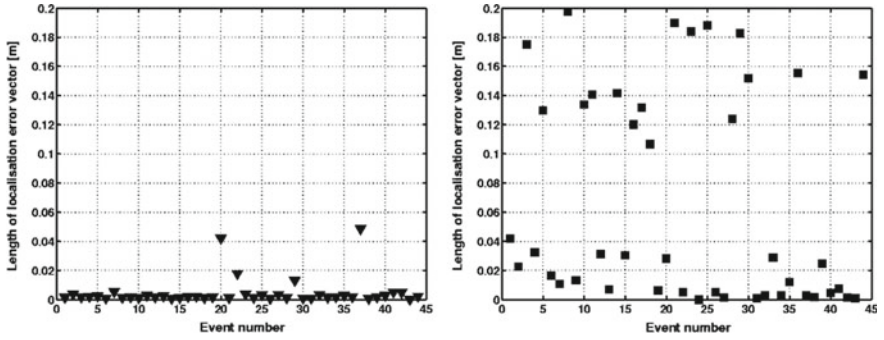

Fig. 3 Length of the mislocation vectors for (left) the comparison of the AIC-picker versus manual picks and (right) the comparison of the Hinkley-picker versus manual picks

is generally recommended for automatic onset determination of AE signals. This can be particularly effective when used in conjunction with source localization schemes that weigh the residuals, as presented in Sects. 5.5 and 5.6. A theoretical discussion and evaluation of arrival-time picking uncertainty can be found in Abakumov et al. (2020).

2.2 Zonal Localization

The simplest way to locate the source of AEs is the so-called *zonal localization method*, where the exact source coordinates are not determined. Here, localization means detecting a signal and the length (or in plate-like structures: the area) in which the source is likely located. As a result, this is the most imprecise localization method. For a particular sensor distribution, the sensor that records the arrival of the elastic wave first is assumed to be the sensor closest to the source. The simplest interpretation is that the source is assumed to be located within a length of $\pm\frac{s}{2}$ of the first-hit sensor, where s is the distance between adjacent sensors. If an AE is detected by multiple sensors, the extracted signal amplitudes can be used to confine the pinpoint location of the source further. An example for the case where the sensors are located along a straight line on a structure is illustrated in Fig. 4. The AE was generated by performing a pencil lead break (PLB).

The left side of Fig. 4 shows a concrete beam (height = 1 m) with eight sensors. The signal emitted from breaking a lead at the surface of the beam and recorded by each sensor is shown on the right side of Fig. 4. Sensors 4 and 5 (numeration top

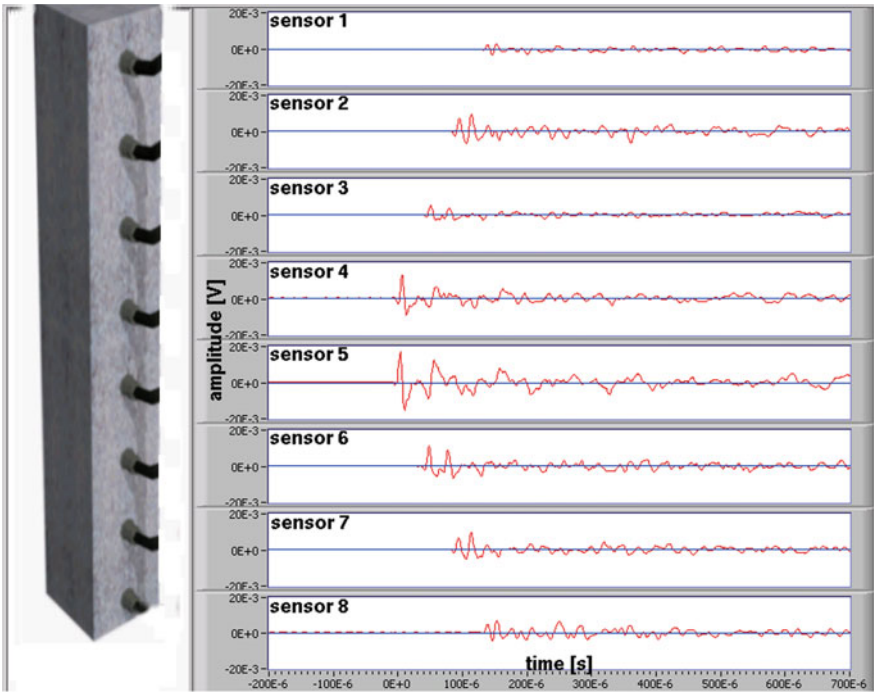

Fig. 4 Sketch of the concrete beam with eight sensors (left) and recorded AE signals from a PLB (right), which was located between Sensors 4 and 5. The amplitude of the signals shows that the source was closer to Sensor 5

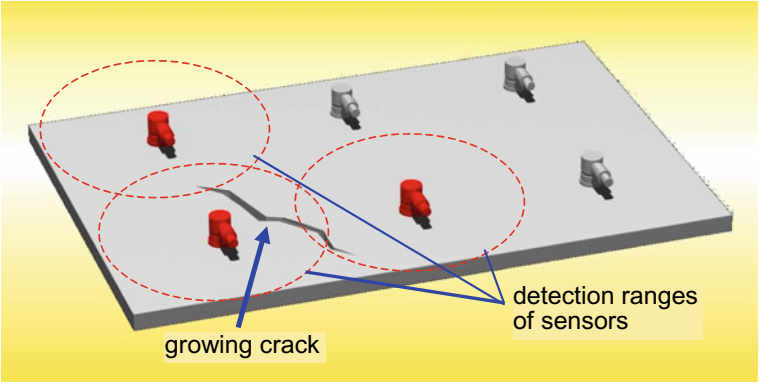

Fig. 5 Sample application of zonal localization for a plate-like structure (Grosse 2005)

down) are the first and second sensors to record the event. This is also the zone of the lead break.

The method of zonal localization can also be applied for plate-like structures, i.e. where the sensors are located on a plane. Figure 5 shows a sample application of zonal localization of a crack in a steel plate.

2.3 One-Dimensional Localization

In this section, one-dimensional (1-D) localization is discussed, which requires at least two sensors in order to calculate a 1-D point between two sensors (Fig. 6) (Reinhardt and Grosse 1999). The geometry of the structure being tested can influence the 1-D localization accuracy. For example, the dimension of a 1-D wire-like structure is significantly larger in one direction compared to the dimensions in the other two directions.

If the distance, s between the two sensors is known, as well as the onset time at each sensor and the wave velocity, v of the material is known, the source time, t_0 and the 1-D source location, x_0 can be calculated. The distances, x_1 and x_2 from the source to the sensors can be expressed as:

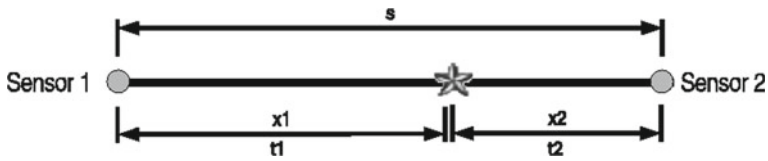

Fig. 6 Principle of a 1-D localization on a wire like structure. The source location is marked by the grey star

$$v \cdot (t_1 - t_0) = x_2 \tag{3}$$

$$v \cdot (t_2 - t_0) = x_1 \tag{4}$$

Knowing x_1 or x_2 the 1-D source localization can be calculated by:

$$s = x_1 + x_2 \tag{5}$$

Inserting Eq. 5 into Eq. 3 or 4 gives a linear system of two unknowns (t_0 and x_1 or x_2) that has to be solved. This gives the source time and the source location relative to the two sensors can now be calculated using Eq. 5.

2.4 Two-Dimensional Localization

The next enhancement in localization accuracy can be achieved by performing a two-dimensional (2-D) localization to determine the coordinates x_0 and y_0 of the source. Since no information about the depth of the source is provided, this technique is sometimes referred to as a *planar localization*. The *planar localization technique* is applied to 2-D structures, where the thickness is small compared to the extent of the object, and the source coordinates are only required in two directions. Another case for using only 2-D localization could be that the sensor distribution is not usable for three-dimensional (3-D) approaches. The equations for 2-D and 3-D localization techniques that use compressional waves are similar and will be handled in the next paragraph. For the case of waves having wavelengths longer than the thickness of the structure, plate or Lamb waves have to be used and their group velocities considered. The 2-D method to determine AE sources is usually applied when the accuracy of the *zonal* technique is insufficient. Applications in civil engineering are reported by authors dealing with the monitoring of large structures like bridge decks (Kapphahn et al. 1993). Kundu (2014) gives an overview of recent developments in AE localization in plate structures and Dubuc et al. (2018) describe an approach using guided waves for AE localization in thin-walled pipes.

In seismology, a 2-D source location with no information about the depth of the event is called epicenter, i.e. the epicenter represents the projection of the seismic source to the earth's surface. At least 3 sensors are needed for a 2-D localization. Assuming constant velocity and three measured arrival times, t_1, t_2 and t_3 of the compressional wave, at three different sensors, the epicenter can be calculated by the hyperbola method (Bath 1979; Pujol 2004). The epicenter must be located on a curve for which the arrival time difference between two sensors, e.g. $t_2 - t_1$ is constant (Fig. 7). Such a curve is a hyperbola with the corresponding sensor coordinates of Sensors 1 and 2 as the foci.

Because generally one arrival time is greater than the other, e.g. $t_2 > t_1$, the epicenter location is limited to one branch of the hyperbola. The hyperbolas of the

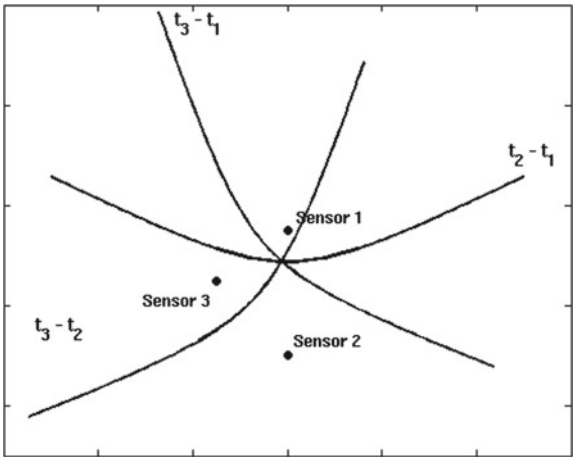

Fig. 7 2-D localization using the hyperbola method. t_1, t_2 and t_3 are the arrival times of the compressional wave at the corresponding sensors

other station pairs (t_1, t_3 and t_2, t_3) are calculated in a similar way. The epicenter is the intersection point of the three hyperbolas (Fig. 7). Due to measurement errors, the three hyperbolas may not intersect at one point (see Sect. 3.5 for more details). For such a case, using more than 3 sensors should improve the localization accuracy and statistical methods must be applied. For example, Joswig (2004) uses a jackknife test to improve the results of the hyperbola method in an overdetermined case.

Besides the hyperbola method, a circle method for 2-D manual localization that uses only the arrival times of the compressional wave can be applied (Bath 1979). Another circle method that requires the arrival times of both the compressional and the shear waves (Havskov et al. 2002) can also be used.

3 High Order Localization Algorithms

3.1 Principal of Computational Localization Techniques

Several authors have worked on high order localization algorithms (Berthelot and Robert 1987; Labusz et al. 1988; Grosse 1996; Köppel 2002; Tarantola 2005). The principal is similar to the determination of earthquake hypocenter s in seismology and uses the arrival of earthquake waves recorded at multiple seismometers. Another approach, which is based on a comparable concept and usable for AE localization, is 3-D positioning using GPS, where travel time differences to the satellites are used (Kurz 2015). These algorithms can be adapted to the requirements in material testing, enabling the study of different specimen geometries, as well as taking into account the number of transducers and their position around the object. The 3-D localization problem is exactly determined when four travel times are available to calculate the

three coordinates and the source time of an event. For a 2-D localization problem to be exactly determined, only three travel times are necessary.

The use of more sensors than unknown source parameters results in the system of equations being overdetermined, and statistical methods such as the methods of least-squares can be used. Usually these methods improve the localization accuracy.

The fundamental concept of that most 3-D localization techniques use is described subsequently. Arrival times are measured at each sensor and used as the reference values for calculated arrival times. The calculated arrival times are computed from a trial or a 'guessed' source location and a user-defined velocity model. The location guess is corrected using the residuals (or difference) between the measured and calculated arrival times, t^c. The calculated arrival time, t_i^c for sensor, i can be written as:

$$t_i^c = t(x_i, y_i, z_i, x_0, y_0, z_0) + t_0 \tag{6}$$

The calculated arrival time, t_i^c is composed of the travel time, t, which is a function of the location of the sensor, (x_i, y_i, z_i), the hypocenter (x_0, y_0, z_0), and the source time, t_0. Since this equation consists of four unknowns, at least four arrival times are needed to determine the hypocenter and the origin time; three arrival times are necessary if only the epicenter and the arrival time are to be calculated. If n arrival times from n sensors are measured, the system is over-determined because there are more knowns than unknowns. An over-determined system has to be solved in a way that the residuals, r_i between calculated and measured arrival time, t_i^0 at each sensor, are minimized.

$$r_i = t_i^0 - t_i^c \stackrel{!}{=} \min \tag{7}$$

Several methods to solve this nonlinear inverse problem are discussed in the following sections.

3.2 Grid Search

In a grid search, the test specimen is discretized or divided into a particular grid, and the travel times from any point in the grid to each sensor are calculated. Since the number of grid points depends on the available computer memory, the grid can be made as fine as what is computationally possible. Comparison of the hypocenter location and the origin time can be used to determine the point of best agreement between the observed and calculated travel times, i.e. using Eq. 7. Several methods can be used to measure the point of best agreement. Each of the methods has case specific advantages and disadvantages and the user should decide from case to case which approach should be taken.

A common approach is the method of least squares (L_2 norm) which leads to root mean squared residuals (where the residual is the difference between the observed and calculated travel times). However, the use of least squares procedures requires the assumption that the distribution of the residuals is of Gaussian nature (Mendecki 1997), which is generally not true. Furthermore, the least squares approach is sensitive to residual outliers, i.e. data points that lie 'far' from the mean or median. Another possibility is to use the variance of the residuals. Since the variance is approximately equal to the mean squared residuals, the problem with the non-Gaussian residual distribution persists and the use of the L_1 norm is preferable. The L_1 norm minimizes the absolute values of the residuals and is less sensitive to outliers. For further approaches concerning the measurement of the best agreement between observed and calculated travel time, refer to Ružek and Kvasnička (2001).

The point having the lowest misfit (L_1 or L_2 norm) is usually the best hypocenter with the corresponding source time. Due to the possibility of there being multiple similar minima, the misfit uncertainties of the solutions should be estimated. One simple possibility is to investigate how the misfit value increases when moving away from the minimum. A criterion for a good solution is a rapidly growing misfit value (Hasvskov et al. 2002).

Dill-Langer et al. (2002) applied a 2-dimensional grid search localization procedure for wood.

Wood is an anisotropic material and therefore the velocity is a function of the angle of wave propagation and fiber direction (Fig. 8). By reducing the full 3D problem to a 2D approximation, the complexity of the localization problem in an anisotropic medium can be reduced. As many wooden building components can be approximated as two-dimensional structures the 2D localization concept may deliver valuable results in many cases.

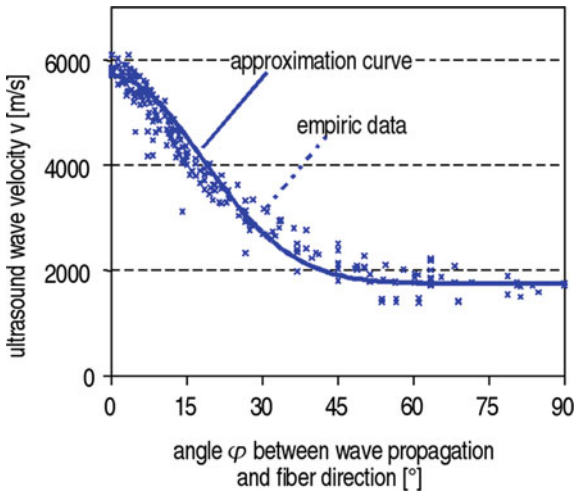

Fig. 8 Empirically determined ultrasound wave velocity as a function of angle φ between propagation and fiber direction

In order to lay the foundations for a verifiable localization of AE sources, the ultrasound velocity of the compressional wave, which depends on the angle between the wave propagation direction and the fiber direction, was measured (Fig. 8).

The investigated material was European spruce lumber (picea abies). The geometry and dimensions of the shoulder-shaped specimens were the following: the width, b_T (perpendicular to grain, defined as x-direction) and the length, l_T (parallel to grain and load direction; defined as y-direction) of the actual test section with reduced cross-sectional width were, $b_T = 120$ mm and $l_T = 500$ mm. The width, b of the clamping sections was 165 mm and the total length, l of the specimen was 2400 mm. Since the thickness of the planed specimen was $d = 25$ mm, which was the distinctly smallest dimension, the structure could be approximated as being a 2-D structure. The test sections of the specimen contained zones with pronounced accumulations of knots. The zone of highest knot density was located approximately at mid-length (Fig. 9).

Briefly summarized, it was found that more than 90% of the calculated source coordinates were located within about ± 8 mm from the actual pulse source location in the x-direction and ± 22 mm in the y-direction (parallel to grain).

Figure 9 gives a graphical overview of the 2-D results of the localized AEs source compared to the location of the natural defects (knots). For the test specimen, the majority of localized AE sources were quite well correlated with the location of the

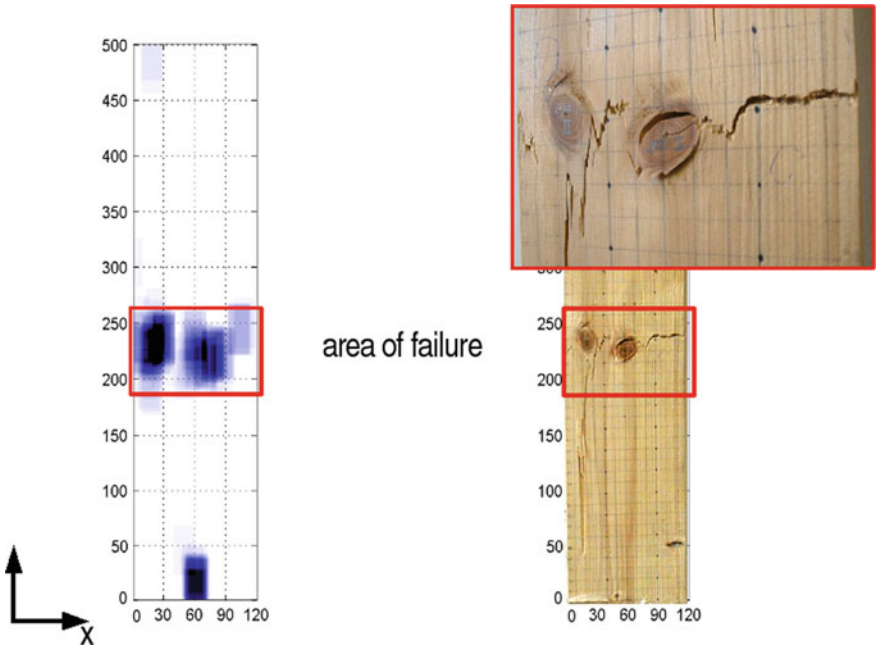

Fig. 9 Comparative representations of AE sources and defects for specimen. Results of 2-D localization of AE sources (left) in form of a density plot and locations of natural and artificial defects (knots) and line of ultimate failure (right)

two main knots near mid-length of the specimen. As anticipated, the vast majority of AE sources were located around the two relatively large knots, where local fiber deviations occurred. The fracture line was complex with both tension and shear modes and was located predominantly slightly above the centers of the localized AE clusters.

The results of the reported tests prove the feasibility of 2-D AE source localization in wooden plane-like specimens, despite the pronounced anisotropy of wave velocities in the plane parallel and perpendicular to the fiber direction and despite some material inhomogenities.

A novel nonlinear approach that can take into account a heterogeneous velocity model as well as non-straight wave propagation paths is described in Gollob et al. (2017). Figure 10 illustrates why the assumption of straight wave travel paths can lead to significant errors: While the difference between the actual and straight wave travel path can be negligible for the case of small distributed air voids ($l_{bp} \approx l_d$), the presence of a discrete crack may significantly increase the actual wave travel path between a source and a sensor ($l_{bp} \gg l_d$). These two cases are illustrated in Figs. 10a, b, respectively. Furthermore, the presence of rock aggregates and steel reinforcing bars introduces heterogeneity and anisotropic behavior, respectively. The proposed algorithm called *FastWay* is capable of handling all of these challenges simultaneously.

In *FastWay*, the structure to be tested is divided into finite cubes (or voxels), of which each has its own velocity. This way, heterogeneity and anisotropy present in a structure can be fully considered. The major difference between traditional AE

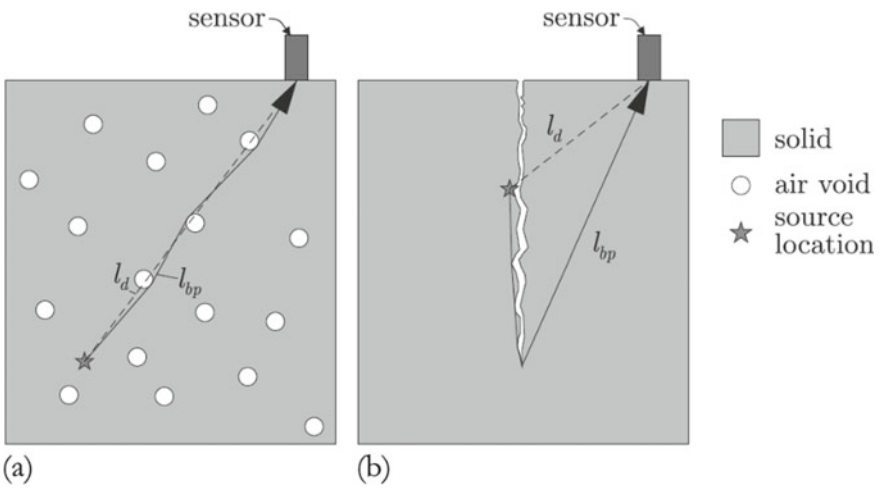

Fig. 10 Illustration of errors made when assumption of straight wave travel paths are used for material with **a** small distributed air voids and **b** a discrete crack. Figure adapted from Gollob et al. (2017)

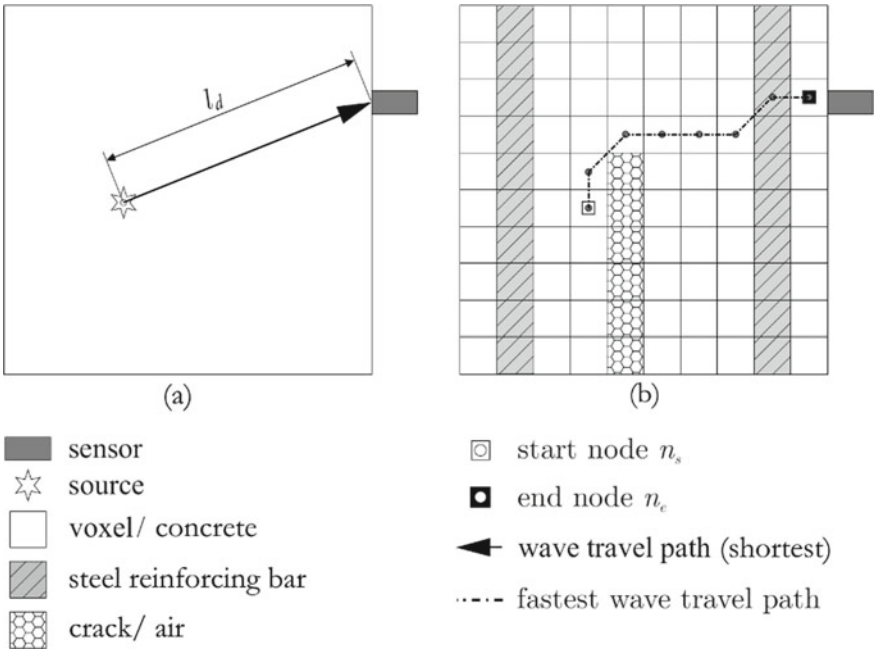

Fig. 11 Illustration of wave travel path assumptions for **a** traditional methods (shortest, straight path) and **b** FastWay (fastest, non-straight multi-segment path)

source localization methods and *FastWay* is that it can consider non-straight multi-segment wave travel paths allowing for the fastest rather than the shortest paths to be used to estimate the location of a source (see Fig. 11). Dijkstra's algorithm (Dijkstra 1959), which is a graphical searching algorithm used to solve single-source shortest-path problems, was modified to compute the fastest path between two voxels. In summary, arrival times are computed for each sensor between the sensor and each voxel in a step-by-step process, in the process mapping the travel paths, as illustrated in Fig. 11b. These maps, in form of matrices, are then used to determine the optimal source location, which is done by comparing the precomputed mapped arrival times with the measured ones. At least four arrival times have to be measured in order to locate an AE source in three dimensions. The voxel associated with the smallest numerical difference is assumed to contain the AE source.

The authors have evaluated FastWay using both numerical as well as experimental tests. An example of a localization result for a simulated concrete prism with a reinforcing bar at the center of the cross section and a vertical crack is provided in Fig. 12. This numerical test specimen was discretized into $5 \times 5 \times 5$ mm voxels, differentiating between concrete, steel, and air. The P-wave velocity for air was set to a near-zero value while concrete and steel were assigned values of 4000 and 4900 m/s, respectively. The relatively low P-wave velocity of steel is justified by the assumption that the rebar acts like a wave guide, therefore having a lower apparent velocity. It can

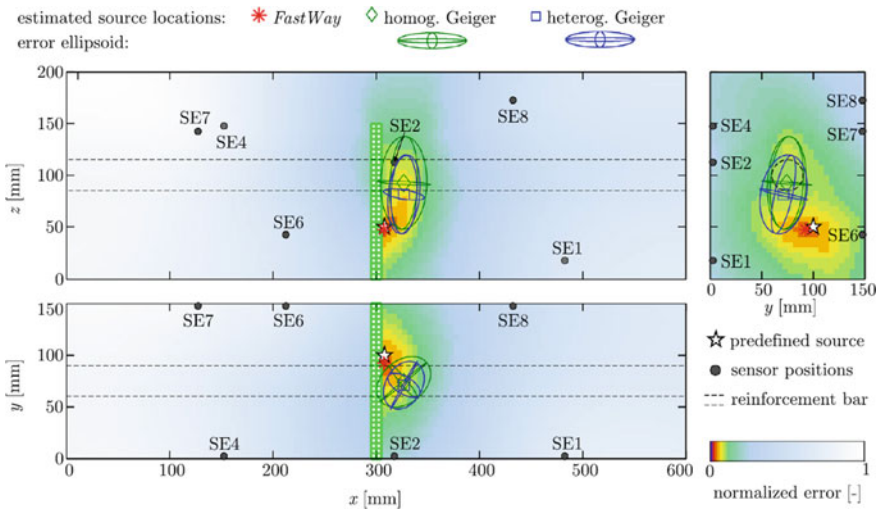

Fig. 12 Localization result for sample AE source in a simulated concrete prism. The green line at the center represents a vertical crack. *Figure source* Gollob et al. (2017)

be observed that *FastWay* is able to pin-point to the simulated source very accurately, despite the crack and reinforcing bar, demonstrating its capabilities. For comparison, the traditional techniques (denoted as Geiger methods) have large errors due to the assumption of straight wave travel paths. The coloring of the specimen corresponds to the normalized error, which can be computed for each voxel. Note that the localization uncertainty of *FastWay* is related to the voxel size, i.e. the source is assumed to be located anywhere in the voxel. Full details of *FastWay* and all conducted tests are provided in Gollob (2017).

While this novel algorithm promises to produce the most accurate source localizations, some limitations should be considered. First, an accurate velocity model needs to be determined, i.e. each voxel needs to be assigned an individual P-wave velocity. While this could be done based on detailed X-ray tomography or MRI images, this would be expensive and prohibitive for larger specimens or in-service structures. Also, the localizations are computationally expensive, requiring significant computer hardware.

3.3 Array Localization

A further approach for 2-D localization of AEs is array localization. The term *array localization* implies that an array (or group) of sensors is used to determine the origin of AEs lying outside this array. In such a configuration the events have usually a large epicentral distance compared to the aperture (extension) of the array – the distance

between the center of the array and the epicenter is usually more than 2–3 times the array aperture.

Array localization typically only provides an estimate of the direction and incidence angle of the approaching elastic wave in the array's plane (Fig. 13). The techniques has found application with wireless sensor nodes to monitor large structures; the sensors of the array can be distributed around one or two nodes and monitor a relatively large area of the structure (Grosse et al. 2006). More details regarding the application of this approach are included in chapter "AE in Masonry". However, the principle of array technology was first applied in electrical engineering (e.g. for antenna arrays) and is also used in seismology (e.g. for monitoring purposes in the frame of the nuclear test ban treaty). Due to the similarity between AE analysis and seismology, and that in both cases elastic waves are investigated, the references of this subsection are mainly of seismologic origin. Schweitzer et al. (2002), Rost and Thomas (2002) and Capon (1969) provide an overview in theory and applications of array seismology and are used as main references for this topic.

In a sensor array numerous sensors are placed at discrete points in a well-defined configuration (Rost and Thomas 2002) as shown in Fig. 13 (right). The idea of installing arrays of sensors is to improve the signal-to-noise ratio. The superior signal detection capability of arrays is obtained by applying *beam forming* techniques, which suppress the noise while preserving the signal, thus enhancing the signal-to-noise ratio (Schweitzer et al. 2002). Furthermore, arrays allow the station-to-event azimuth, called the back-azimuth, to be estimated.

The array methods presented here assume that a plane wave arrives at the array. The wave must have traveled a certain distance depending on the wavelength for this assumption to be acceptable. The direction of a propagating elastic wave can be described by the vertical incidence angle, i (Fig. 13, left) and the back azimuth, Θ

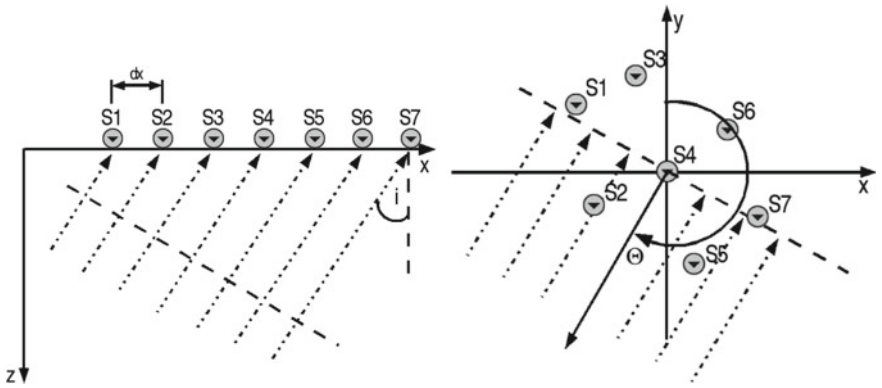

Fig. 13 *Left*: cross section of the incident wave front (dashed line) crossing a linear array of 7 sensors (S1–S7) at an incidence angle, *i*. *Right*: horizontal plane of an incident plane wave front (dashed line) arriving with a back-azimuth, Θ relative to the reference Sensor S4 at an arbitrary array of 7 sensors (S1–S7)

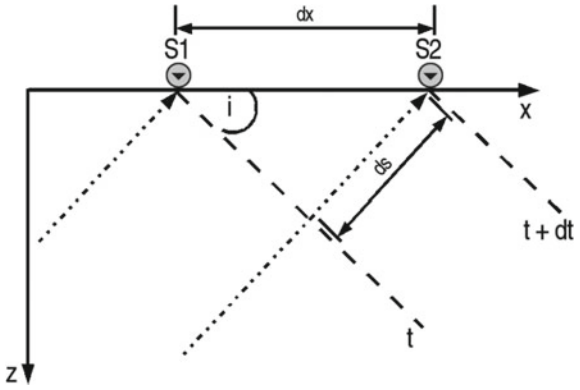

Fig. 14 Plane wave front incident on a surface with two sensors (S1 and S2). The angle i is the incidence angle defined in Fig. 13 (left)

(Fig. 13, right) which is measured relative to a designated reference sensor (here: S4 in Fig. 13, right) in the array.

In practice, the incidence angle, i is not used, but the apparent velocity, which is derived subsequently. The wave fronts arriving at, for example, two sensors at time t and time $t + dt$ are separated by distance ds along the raypath (Fig. 14). The distances dx and ds are related to the incidence angle through (Shearer 1999):

$$ds = dx \cdot \sin i \tag{8}$$

Assuming a uniform velocity in the material, $v_0 = ds/dt$, Eq. 8 can be rewritten as:

$$v_0\, dt = dx \cdot \sin i \tag{9}$$

Equation 9 can be rearranged as:

$$\frac{dt}{dx} = \frac{\sin i}{v_0} = s \tag{10}$$

The slowness, s is the inverse of the apparent velocity of the wave front crossing the array and defined as $v_{app} = dx/dt$. The apparent velocity is a constant for a specific ray travelling through a material. If the slowness vector, $\mathbf{s} = (s_x, s_y, s_z)$ is used rather than the absolute value of the slowness s, the components of the slowness can be expressed as functions of the back-azimuth, Θ and the incidence angle, i (Rost and Thomas 2002):

$$s = \left(\frac{\sin \Theta}{v_{app}}, \frac{\cos \Theta}{v_{app}}, \frac{1}{v_{app} \tan i} \right) \tag{11}$$

Sensor arrays, as presented here, are used for the separation of coherent signals and noise. The basic method used to separate the coherent and incoherent parts of a signal

is known as 'array beam forming'. Array beam forming enables the determination of the back-azimuth of the incident wave. One sensor is chosen as a reference sensor and all parameters are taken relative to this sensor (Fig. 14).

For most applications all sensors are in the same plane. In such a case, the vertical component of the slowness vector, s_z is zero. The special case where not all sensors of the array are in one plane is considered in Schweizer et al. (2002).

The beam forming method uses the differential travel times of the plane wave front for each source-receiver combination and depends on the particular slowness and back-azimuth to individual array stations. Therefore, the main goal of array beam forming is to find the best delay times for shifting the individual signals. If the single-sensor recordings are appropriately shifted in time, for a certain back-azimuth and slowness, all signals with the matching back-azimuth and slowness will sum constructively (Rost and Thomas 2002). The delay times, τ_j are the sensor position vector, $\boldsymbol{r}_j$ (relative to the reference sensor) multiplied by the slowness vector, $\boldsymbol{s}$:

$$\tau_j = r_j \cdot s \tag{12}$$

The complete geometrical derivation of Eq. 12 for the sensors of an array can also be found in Schweitzer et al. (2002).

An array beam, *B(t)* can be calculated using the following formula:

$$B(t) = \frac{1}{M} \sum_{j=1}^{M} R_j\left(t + \tau_j\right), \tag{13}$$

where $R_j(\boldsymbol{r}_j, t)$ is the digital sample of the signal from sensor, j at time, t. Figure 15 shows an example of beam forming. The top trace shows an array beam that results from applying the beam forming method to the other eight channels. This example shows how the signal-to-noise ratio can increase during beam forming. The signal-to-noise ratio of the array increases with the square root of the number of sensors of the array and is significantly higher than the signal-to-noise ratio of a single sensor (Rost and Thomas 2002).

When AEs are localized with a sensor array, the back-azimuths of the propagating elastic waves are determined. The true beam can only be calculated for the correct back-azimuth. However, the back-azimuth is the parameter we want to determine. Equation 12 shows that any delay time for each sensor can be calculated by multiplying the coordinates of each sensor with a slowness vector. Since the slowness is a function of back-azimuth and incidence angle (Eq. 11) it is possible to calculate the true beam by beam forming calculations on a grid of different slowness values. More specifically, a grid of s_x and s_y values is defined and for every combination of the horizontal slowness values, the energy of the beam (integrating over the squared amplitudes) is calculated. The maximum energy indicates the true beam since only the coherent signals of a phase (e.g. compressional wave) superimpose constructively. Searching for the true beam can be performed in the time domain, where the

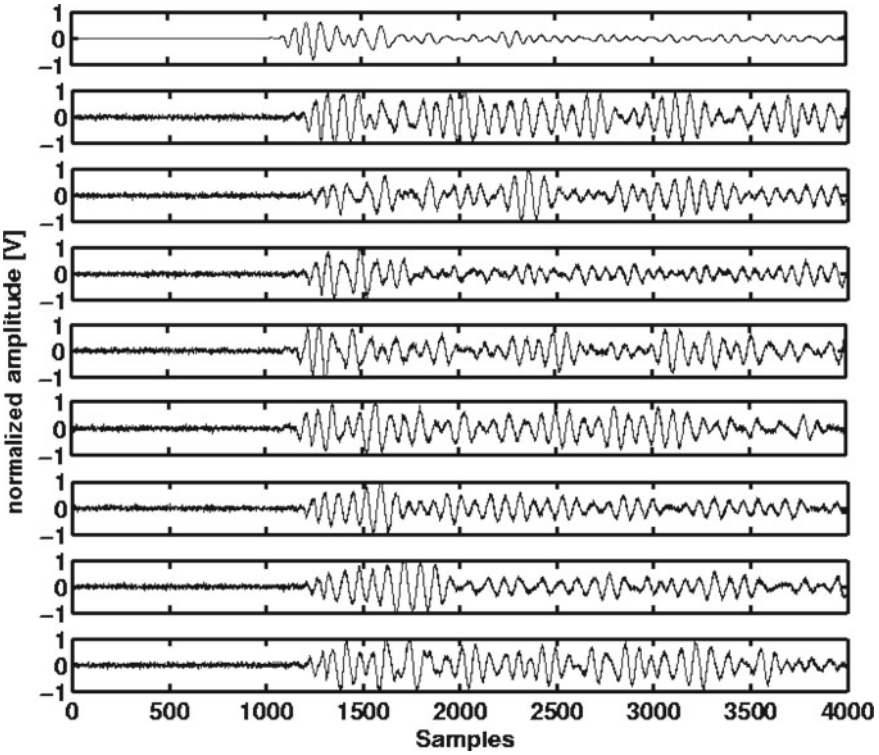

Fig. 15 Beam forming example, where the top trace is the beam of an artificial AE source. Note the higher signal-to-noise ratio of the top trace compared with the traces below, which correspond to the individual sensor measurements

method is called 'beam packing' (Fig. 16, left) and in the frequency domain, where it is referred to as 'frequency wavenumber analysis' (Fig. 16, right).

Beam packing is directly applied to the signal in the time domain. Since a time shift in the time domain is equivalent to a phase shift in the frequency domain, beam packing is equivalent to frequency-wavenumber (f-k) analysis. The f-k analysis has the advantage that its numerical calculation is faster than the corresponding procedure in the time domain and it is more accurate.

The total energy of a record at an array is defined as:

$$E = \int_{-\infty}^{\infty} B(t)^2 dt = \int_{-\infty}^{\infty} \left[\frac{1}{M} \sum_{j=1}^{M} R_j(t + \tau_j) \right]^2 dt \tag{14}$$

Using Parseval's theorem (Brigham 1974), Eq. 14 can be written in the frequency domain:

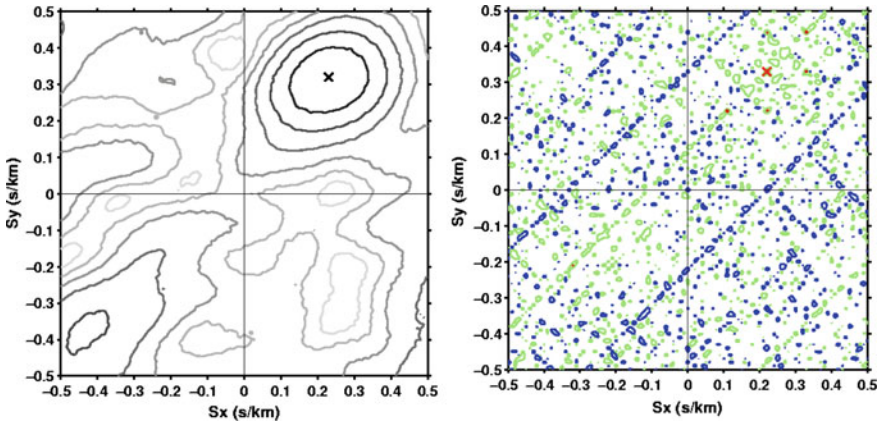

Fig. 16 Calculation of the back-azimuth of the same incoming wave using the beam packing method (left) and f-k analysis (right). The cross indicates the calculated maximum energy for particular slowness values, s_x and s_y. The back-azimuth is the angle between the center of the coordinate plane and the point of maximum energy

$$E(\omega, \mathrm{k} - \mathrm{k}_0) = \int_{-\infty}^{\infty} |B(\omega)|^2 \left| \frac{1}{M} \sum_{j=1}^{M} e^{i\omega r_j k} \right|^2 d\omega \tag{15}$$

where $\boldsymbol{B}(\omega)$ is the Fourier transform of $B(t)$. The wavenumber vector, $\boldsymbol{k}$ is defined as $\boldsymbol{k} = \omega \cdot \boldsymbol{s}$. The back-azimuth is calculated from an f-k diagram or a beam packing diagram in the following way. It is assumed that the incident wave travels through an imaginary half sphere beneath the array to a particular point. The half sphere is projected to the surface in the corresponding diagram. Therefore, the slowness and wavenumber are measured in polar coordinates and the back-azimuth can be calculated as:

$$\Theta = \tan^{-1}\left(\frac{k_x}{k_y}\right) = \tan^{-1}\left(\frac{s_x}{s_y}\right) \tag{16}$$

A detailed description of the f-k analysis can be found in, for example, Capon (1969), Smart and Flinn (1971) or Aki and Richards (1980).

Figure 17 shows a sketch illustrating the principle and results of a typical array experiment. Three different source points of artificial sources were chosen, which are marked by black crosses in Fig. 17, top left. The f-k analysis of the data from the source perpendicular to sensor S_1 shows that the back-azimuth is zero degrees (star in Fig. 17, top right). The measured back-azimuth agrees exactly with the true value. This is not the case for the two source points near the edges of the concrete plate. Due to reflections from the sidewalls, the back-azimuth determined from the data of the source on left side differs by an amount of 4.9° from the true value and the one

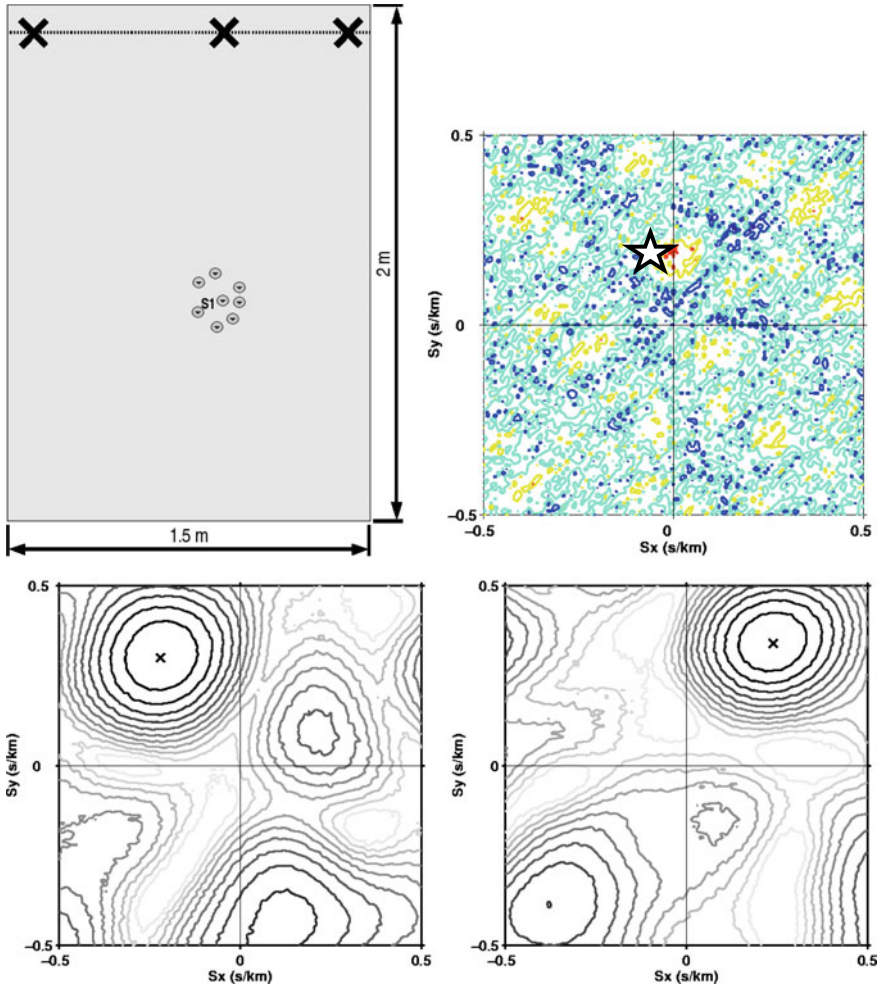

Fig. 17 *Top left*: sketch of a typical array experiment. A sensor array, with reference sensor S_1, is placed on a concrete plate (2 m × 1.5 m × 0.3 m). Artificial sources (pencil lead breaks or small impacts) are generated at one side of the concrete plate. The source points are marked by black crosses. *Top right*: *f-k* analysis of the data from the source point perpendicular to sensor S_1. The maximum energy is marked by a cross. *Bottom left and bottom right*: results of the beam packing analysis of the data from the left source point (left) and from the right source point (right). The maximum energy is again marked by a cross

of the right side differs by 3.7° from the true value. For comparison, a beam-packing analysis was also applied (Fig. 17, bottom). In addition, the array geometry can also have an influence on the results because the quality of the results can depend on the direction to the source. If more than one array is used, a 2D localization of the source

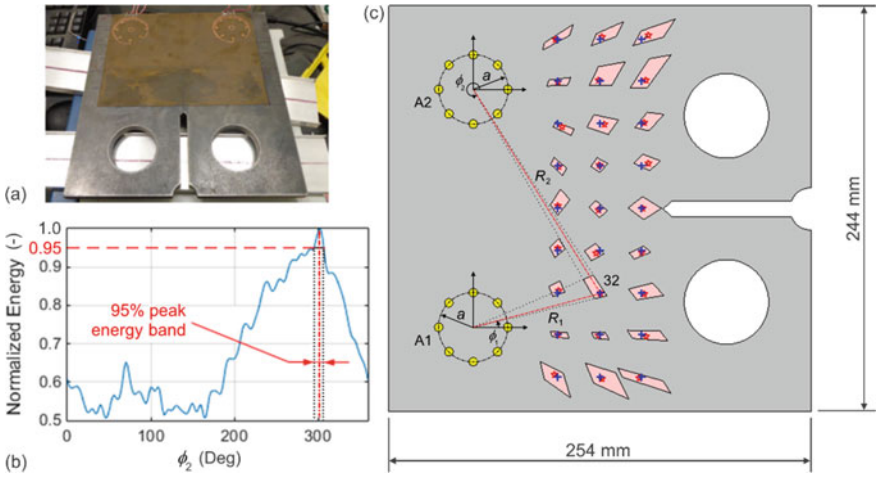

Fig. 18 **a** Photo of the steel test specimen with two circular sensor arrays, **b** beam energy as a function of incidence angle for Array A2, including proposed 95% peak beam energy uncertainty measure, and **c** results of all localized pencil lead breaks (PLB). Blue '+' and red stars represent actual and mean estimated PLB locations, respectively. The pink quadrilaterals represent the area of uncertainty. R_i is the distance between an array's reference point and the source location. Figure adapted from Mhamdi and Schumacher (2015)

of the incident wave can be applied, by calculating the point of intersection of the two back-azimuth lines.

One of the limitations of traditional array localization, which uses a single array, is that only the direction (or back-azimuth) of a source can be estimated with sufficient accuracy. Mhamdi and Schumacher (2015) propose the use of two circular arrays to determine the intersection of two back-azimuths, which represents the pinpoint location of the source, to overcome this limitation. Figure 18a shows a photo of the laboratory test specimen, which was made of structural steel having a geometry following ASTM E647-11. The two sensor arrays consisted of eight lead zirconate titanate (PZT) piezoelectric discs, each arranged in a circle with a diameter, $a =$ 30 mm. The PZT discs had a diameter and thickness of 5 and 0.4 mm, respectively, with a resonant frequency of 450 kHz. A printed circuit board (PCB) provided the electrical connections between the PZT discs and the data acquisition system (DAQ). PLBs were performed at 27 select locations lying outside of the array, shown with blue '+' in Fig. 18c. For each PLB location, mean incident angles, ϕ for both arrays (i.e. A1 and A2) using time history-based beam packing as discussed earlier in this section. The centers of the circular arrays were assumed as the array reference point and incident angles were computed counter-clockwise from the local x-axes. In order to represent a measure of location uncertainty, the 95% peak beam energy band was proposed, as illustrated in Figs. 18b, c shows mean estimated PLB locations with a red '*' and the pink quadrilaterals represent the area of uncertainty. The authors compared the mean location estimates with the ones obtained using a traditional

2-D localization technique discussed in Sects. 2.3 and 4.1. They found that the absolute source location errors using the proposed array-based approach were overall significantly smaller. The array-based approach outperforms the traditional technique in particular for locations that lie outside of the array, which is expected, as traditional localization techniques are known to produce large errors for sources that lie outside of the sensor array. Finally, it should be noted that the phased array approach worked accurately even for PLB sources that were close to the array, i.e. approaching $R/a \approx 2$, where the plane wave assumption is theoretically not appropriate.

3.4 Iterative Localization

The standard technique for 3-D localization is to linearize the problem. The standard equations used to calculate a 3-D location (hypocenter or source of an AE) are based on the assumptions that the material is homogeneous and isotropic and that the AE source resembles a point source. If this is not the case, the following approach has to be modified.

3-D localization requires the onset times from at least four sensors. The most common approach is to use an iterative localization algorithm, which requires the linearization of the problem. To do this, a 'first guess' or trial hypocenter (x_0, y_0, z_0, t_0) is required. This first guess hypocenter must lie relatively close to the true hypocenter, which is not known. The travel time residuals r_i of the first guess hypocenter are then a linear function of the correction in hypocentral distance (Havskov et al. 2002).

For smaller specimens, the middle of the specimen is an adequate choice for the first guess hypocenter. For other cases the center of the sensor network should be chosen. For larger specimens, the sensor which recorded the event first can be chosen.

Assuming that the material is homogeneous and isotropic, the travel times for 3-D localization can then be calculated using (see also Eq. 6):

$$t_i = \frac{\sqrt{(x - x_i)^2 + (y - y_i)^2 + (z - z_i)^2}}{v} + t_0 \tag{17}$$

The source coordinates, (x, y, z) represent the point for which the travel time to each sensor location, (x_i, y_i, z_i) is calculated, i.e. the first guess of the hypocenter. The bulk wave velocity of the material is denoted by v and t_0 is the first guess origin time, which is taken as the center point of the specimen.

Due to the first guess hypocenter being a trial solution, the calculated travel time s differ from the measured ones. A correction vector, $\Delta\mathbf{x}(\Delta x, \Delta y, \Delta z, \Delta t)$ is computed based on the first guess hypocenter to minimize the travel time residuals (see also Eq. 7). If the necessary corrections are relatively small, the travel time function (Eq. 17) can be linearized. Therefore, Eq. 17 can be approximated by a Taylor series, from which only the first term is used. Equation 7 can be rewritten as:

$$r_i = \left(\frac{\partial t}{\partial x_i} \cdot \Delta x\right) + \left(\frac{\partial t}{\partial y_i} \cdot \Delta y\right) + \left(\frac{\partial t}{\partial z_i} \cdot \Delta z\right) + \Delta t \tag{18}$$

In matrix form this is:

$$\mathbf{r} = \mathbf{G} \cdot \Delta\mathbf{x} \tag{19}$$

G is the matrix of partial derivatives and $\Delta\mathbf{x}$ is the correction vector. Due to the source time correction term, the last column of this matrix is always 1. As an example, the partial derivative of the *x*-component of Eq. 17 is:

$$\frac{\partial t_i}{\partial x} = \frac{(x - x_i)}{v} \cdot \frac{1}{\sqrt{(x - x_i)^2 + (y - y_i)^2 + (z - z_i)^2}} \tag{20}$$

To calculate the correction vector, Eq. 19 is solved by matrix inversion, e.g. by calculating the Moore-Penrose generalized matrix inverse:

$$\Delta\mathbf{x} = \left(\mathbf{G}^T\mathbf{G}\right)^{-1}\mathbf{G}^T\mathbf{r} \tag{21}$$

If more than four sensors are used, this procedure is repeated and the correction vector is minimized iteratively. Convergence criteria can be set for terminating the iteration when a particular desired accuracy has been reached, or if the procedure is diverging.

This localization algorithm also provides the possibility to correct the body wave velocity iteratively. To do this, velocities are calculated from the travel time of all events (e.g. recorded during a certain period of the experiment) and the distance calculated between sensor and hypocenter. The linear extrapolation of all these calculated velocities gives a new average velocity for the localization. This procedure can be performed iteratively, in combination with the localization.

The solution can be further stabilized by introducing a weight matrix, **W** to Eq. 19 (Thurber and Engdahl 2000). The data can be weighted according to the quality of the recorded AE signals, sensor-source distance etc. The diagonal elements of the weight matrix are equal to the square root of the weight value, which is normally between 0 and 1:

$$\mathbf{Wr} = \mathbf{WG} \cdot \Delta\mathbf{x} \tag{22}$$

3.5 Localization Errors

An error analysis is necessary for assessing the accuracy and reliability of any localization result. There are different sources of errors that are not clearly separated. Uncertainties in the determination of the arrival times generally depend on data

quality, and how impulsive onsets are. In the presence of noise, low amplitude onsets are easily overlooked. Estimated onset times then are too late or even according to wrong phases. Moreover, the widely used assumption of a homogeneous behavior of the wave propagation may not be correct for a tested structure.

For the iterative linearized localization method presented in Sect. 3.4, localization errors are described by the symmetric covariance matrix **C**. In order to compute **C**, at least five sensors (for the case with four unknown source parameters) with corresponding onset times are required. For the least-squares inversion method, **C** can be readily calculated from **G**, as (Flinn 1965):

$$\mathbf{C} = \sigma_d \left(\mathbf{G}^T \mathbf{G}\right)^{-1} \tag{23}$$

where σ_d is the data variance of the arrival times. The diagonal elements of **C** contain the variances of the source coordinates in the direction of each coordinate axis. Only spatial errors are of interest, which can be visualized by a 3-D-error ellipsoid (Fig. 19). Its shape is defined by the eigenvectors and eigenvalues of **C**, which give its orientation as well as its dimensions. For the 68%-error ellipsoid, the square of the semi axis is given by scaling the eigenvalues by 3.53 (Press et al. 1992).

It is important to note that for a homogeneous material the shape of the error ellipsoid is determined by geometrical relationships between source location and sensor distribution only, as summarized in the matrix, **G** of the partial derivatives (Eqs. 16 and 17). The data uncertainty, σ_d is assumed to obey Gaussian statistics and acts as a scaling factor for **C**.

In the case where AE are expected to occur in certain regions of the test object, different sensor arrangements should be evaluated to enable accurate localization of these AE sources or to determine where additional sensors should be placed. Localization accuracy is highest for events that have appropriate azimuthal coverage by the sensors. This can be illustrated by the following theoretical example where four sensors, arranged in a square, are used to localize AE sources in two dimensions. The arrangement is overdetermined allowing for error analysis. Assuming an AE source

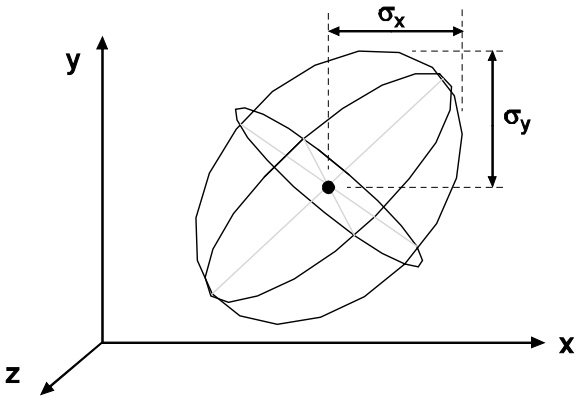

Fig. 19 3-D-error ellipsoid for visualization of the spatial localization error s. Errors, σ_x, σ_y and σ_z can be found as the projections of the ellipsoid in the direction of *x*, *y* and *z*, respectively

with a known location and time of origin, the arrival time s at the four sensors can be calculated with the given wave velocity, υ. Inserting these arrival times into Eq. 16 yields three independent equations which can each be plotted as hyperbolas. These intersect in one point, representing the AE source location as depicted in Fig. 20, left. The top left figure shows a source that lies within and the bottom left figure a source that lies outside the sensor array. In real applications, the arrival times contain some amount of uncertainty and the hyperbolas will not intersect in one point but rather an area. In the present example this is simulated by adding random errors between +5 and –5 μs to the calculated arrival times. Figure 20, right demonstrates the effect

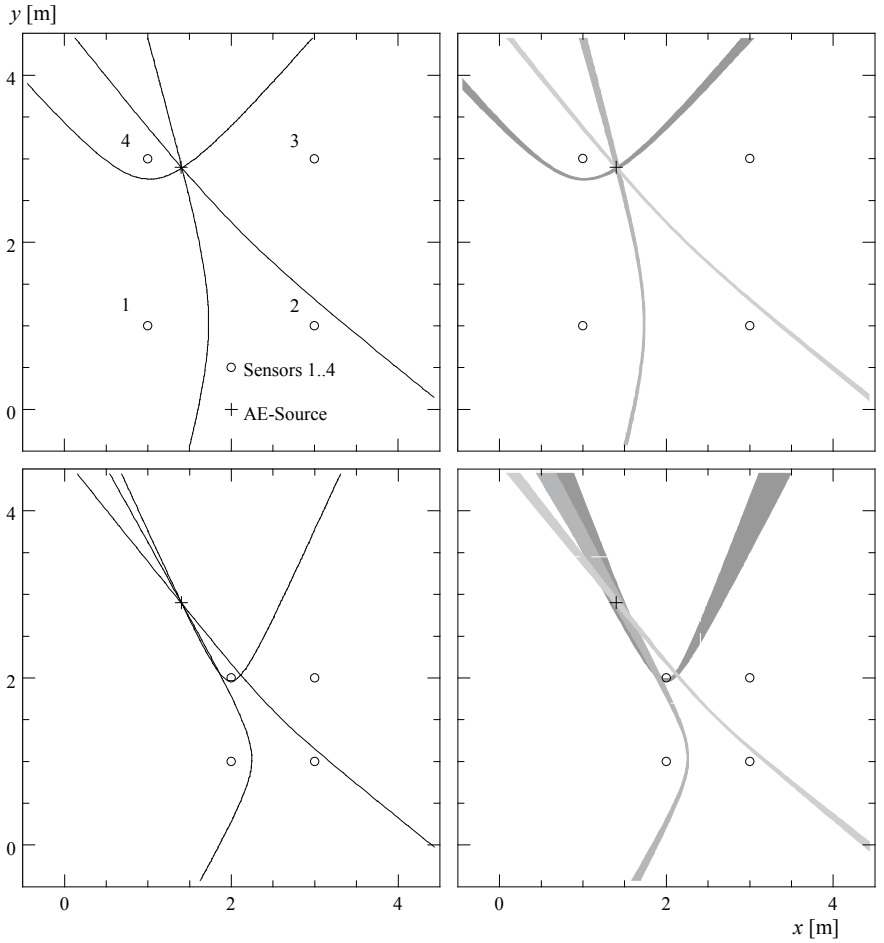

Fig. 20 Theoretical example to demonstrate the effect of the sensor arrangement on the localization accuracy. *Top row*: AE source within sensor array; *bottom row*: AE source outside sensor array. *Left column*: accurate arrival times; *right column*: arrival times with an error of ± 5 μs. Wave velocity, $v = 4500$ m/s

of the sensor arrangement on the localization result. In the diagram below, where the AE source lies outside the sensor array, the hyperbolas intersect in a much larger area compared to the case where the AE source lies within the sensor array.

In principal, the variances of the arrival time data are unknown unless they are estimated for each signal by visual inspection of the waveforms. However, it is possible to estimate σ_d^2 from the remaining discrepancies between observed travel times t_i^0 and calculated travel times t_i^c after source localization, divided by the degree of freedom of the problem with four unknown source parameters. For n observations it is

$$\sigma_d^2 = \frac{1}{n-4} \sum_i \left(t_i^0 - t_i^c\right)^2. \tag{24}$$

Thus it is possible to visualize the localization results and to interpret them according to their location uncertainties by defining a maximal spatial error as the length of the major axis of the error ellipsoid.

Using the same theoretical example as mentioned above, Fig. 21 illustrates the effect of a systematically erroneous arrival time on the source localization. For an array of 40 by 40 AE sources, the theoretical arrival times at the four sensors were calculated. To introduce an error, 5 μs were added to the arrival times of Sensor 1. The iterative localization algorithm then yields AE-source locations that minimize the travel time residuals and thus distribute the error in arrival times over all sensors. Figure 21, top depicts the difference between the actual and the calculated AE-source location, on the left side as error vectors and on the right side as a density function of the error value. Figure 21, bottom left shows a density function of the minimized travel time residuals (mean value over all sensors) and bottom right the major axis of the error ellipsoid. In most cases the size and orientation of calculated location uncertainties (bottom right) corresponds well to the actual error vector (top left).

Whether the calculated value of σ corresponds to the usually unknown actual localization error, depends on the source of error. While inaccurate localization results due to erroneous arrival time determinations or sensor locations are well recognized by high values of σ, a false assumption of the wave velocity, υ leads to low σ but nonetheless wrong localization results. In practical application the value of σ still proves to be the best indicator to distinguish reliable from erroneous localization results.

4 Applications and Practical Considerations of the Iterative Localization Method

AE source localization is used for a wide range of field applications as well as in research. In field applications it is typically part of a monitoring process of civil engineering structures allowing, for example, to detect and localize wire breaks in

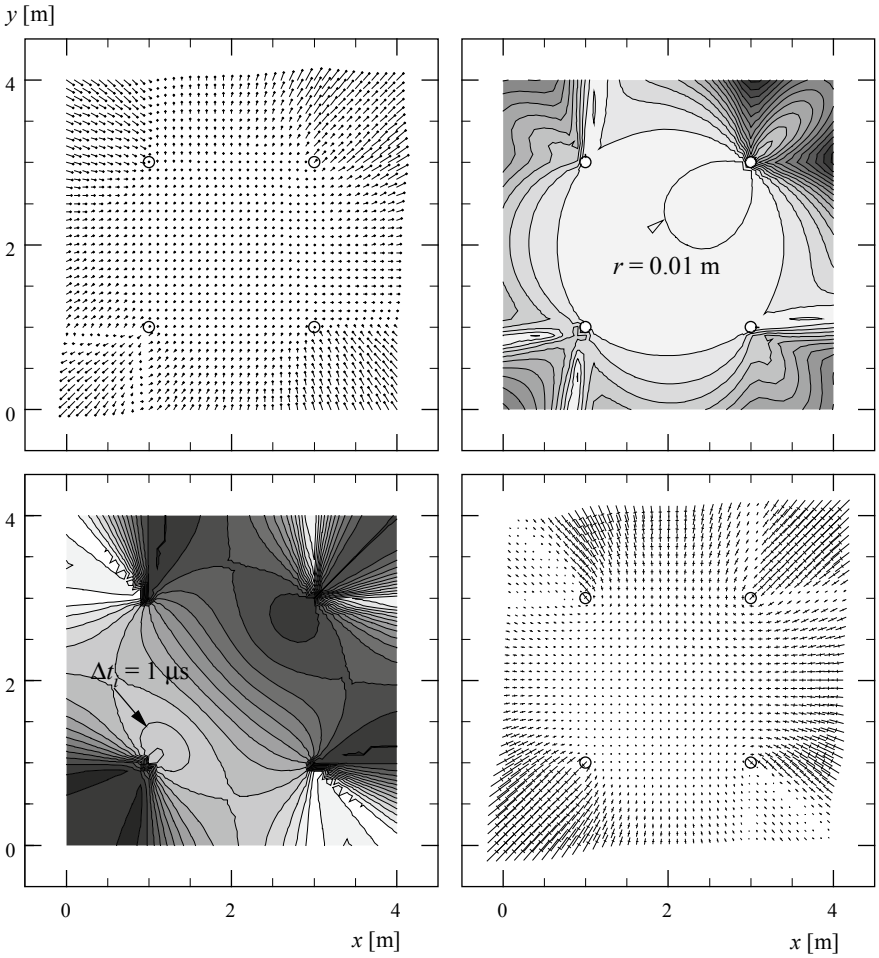

Fig. 21 Localization errors resulting from an erroneous arrival time (same arrangement as Fig. 20, arrival time at sensor 1 altered by 5 µs) calculated and depicted for an array of 40 by 40 points. *Top left*: actual localization errors as vector; *Top right*: actual localization error s as density function (equidistance: 0.01 m); *Bottom left*: mean arrival time residuals as density function (equidistance: 0.25 µs); *Bottom right*: major axis of the error ellipsoid

cable stay bridges (1-D localization), in prestressed decks or in bridge girders (2- or 3-D localization). In research applications, source localization is often required as a prerequisite for quantitative AE analysis with the aim of observing fracture processes within the specimen or component (see chapter "Signal-based AE Analysis").

The requirements for the testing equipment i.e. sensors and acquisition unit are relatively low. At the same time the interpretation of the results is—at least at first sight—unambiguous and requires little understanding. AE source locations can easily be depicted for example in a plan view of the observed structure. Commercially

available analysis software or entire testing units allowing for the online localization of AE sources are usually based on the iterative localization method described in Sect. 3.4.

4.1 Reliability and Accuracy

In practical applications AE source localization is often applied to large amounts of data. In order to interpret the result it is crucial to recognize erroneous source locations and concentrate on the reliable portions of the data. As discussed in Sect. 3.5, this distinction can, for example, be achieved based on the variance, σ of the location result.

The AE source locations depicted in Fig. 22 were collected during pullout tests on concrete cubes of 200 × 200 × 200 mm with a rebar Ø 14 mm embedded centrically and bonded only over the length of Ø 3 mm (Köppel and Vogel 2000; Köppel 2002). During pullout, AE signals were recorded on eight sensors mounted on the concrete surface. Figure 22, left displays 3639 AE events recorded on all eight channels and localized with the iterative localization method described in Sect. 3.5. While failure was observed in the bond region of the rebar only, AE events were localized throughout the specimen i.e. also in places where the occurrence of cracks is highly unlikely. The brightness of the dots marking the AE location indicates their accuracy. Localization results with a high variance, σ, i.e. a low accuracy, are marked in light gray and localization results with a low variance σ in black.

In Fig. 22 it can be observed, that the localization results with a low σ tend to be located around the boundary between rebar and concrete, which is where AE sources are expected in this test. If a high number of AE locations are available,

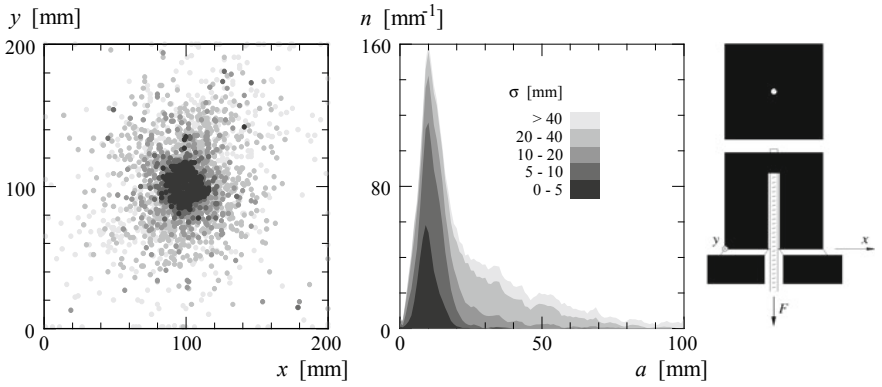

Fig. 22 AE source locations of 3639 AE events obtained during a pullout test. The variances, $\sigma = 1/3(\sigma_x + \sigma_y + \sigma_z)$ of the location results are indicated via gray tone. Plausible AE sources in the bond region correspond to AE-Source locations with a low σ

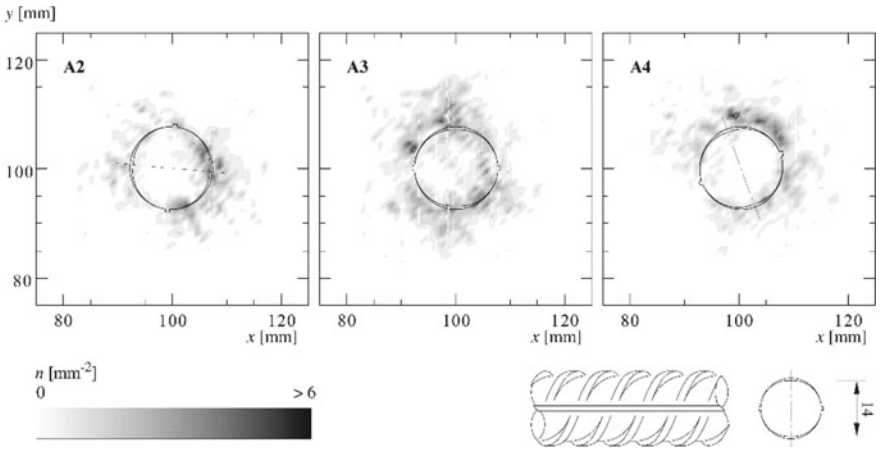

Fig. 23 Localization results of three pullout tests displayed as density functions. Regions of high AE activity correlate with the ribs of the rebar

displaying only those with low σ increases the reliability of the result and facilitates the interpretation.

If regions (or clusters) of high AE activity rather than the exact location of single events are of interest, visualizing localization results as density functions instead of data points facilitates the interpretation. Assuming erroneous localization results to be distributed uniformly while correct locations are concentrated in actual fracture regions, this procedure increases also the accuracy of the result. In Fig. 23, the AE locations of three pullout tests are displayed as density function s. It can be observed that AEs are located in the bond region and clearly concentrated at the ribs of the rebar.

4.2 Limitations

Like all high order localization methods, the iterative localization method works with arrival times of certain wave types like P-waves, S-waves, surface waves or Lamb waves. A complex test specimen with irregular boundaries and an inhomogeneous structure causes reflections or scattered waves, which interfere in the signal and thus have no obvious onsets. The first onset usually is the clearest one and is therefore in most cases used for the localization. It corresponds to the compressional P-wave, which has the highest propagation velocity, but may not be detectable in a noisy environment or over long distances in concrete due to its relatively high attenuation.

As a result, AE sources can only be reliably localized over a limited distance and as long as the assumption of a homogenous media is valid for the considered wavelength. While inhomogenities due to the reinforcement or tendons have limited impact on the localization result, crack s may introduce wave barriers and thus restrict

the regions where localization is possible. AE sources beyond existing cracks can typically not be localized. The following two examples of large-scale laboratory experiments demonstrate this effect.

The AE localization results displayed in Fig. 24 were recorded during the loading of a 21 m long prestressed bridge girder (Köppel and Vogel 2000; Zwicky and Vogel 2000). This member was removed from a bridge and subjected to a three-point-bending test in an outdoor facility at the ETH Zürich. To provoke shear failure, the load was applied close to one of the support. AE were recorded by eight sensors located in close vicinity on both sides of the girder in the shear region.

All AE sources localized with a satisfying accuracy, i.e. with a variance $\sigma <$ 15 mm, can be attributed to the two cracks adjacent to the sensor array. AE sources originating from beyond those cracks could not be properly localized.

As another example for the application of the iterative localization method, location results of AE during the loading of a reinforced concrete beam are documented by Schechinger (2005). An overview of the test setup can be seen in Fig. 25 (top). The specimen had a cross section of 440 × 440 mm and a total length of 4.50 m. The beam was assembled with four steel reinforcement bars of 22 mm diameter and an

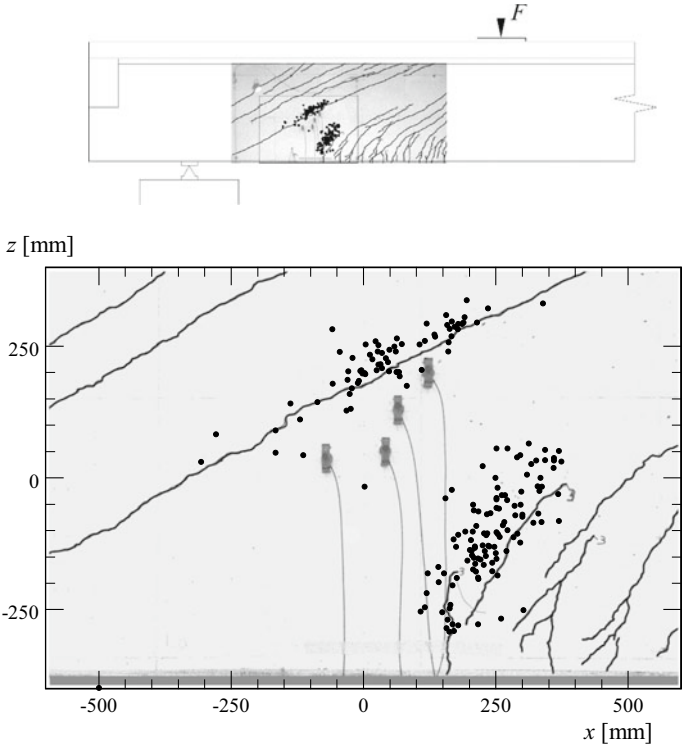

Fig. 24 AE sources registered and localized during the three-point bending of a 21 m long prestressed bridge girder. Depicted are only localization results with $\sigma < 15$ mm

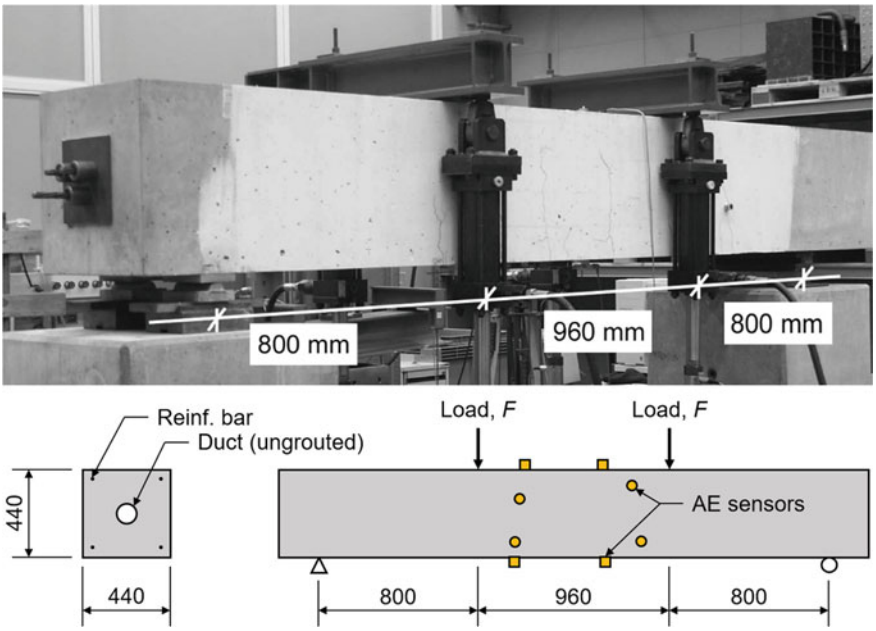

Fig. 25 Overview of the four-point-bending experiment (top), cross section of the reinforced concrete test beam (bottom left side) and elevation view of the experimental setup (bottom right side). All measurements in (mm)

ungrouted steel duct of 93/99 mm diameter located at the center of the cross section (Fig. 25, bottom left side). The experiment was carried out as a symmetric four-point-bending test, as shown in Fig. 25 (bottom right side). The maximum bending stress occurred between the two loading points on a length of 0.96 m. In that region, eight AE sensors were mounted to the concrete surface to record AE signals from the expected bending cracks. AE events were localized if arrival times of at least six sensors were available.

Figure 26 shows the localized AE events that occurred from the initial loading up to the time when the cracking load was reached. First hairline crack s were visible on the bottom side where the bending causes tension of the concrete. Only those results are displayed that satisfy a selected criterion for "good localization", which here is that the mean residuum for each event has to be smaller than 10 μs. Localized AE coincide with the topography of two evolving cracks. Results from a later loading step, where sudden crack growth occurred, are shown in Fig. 27. Numerous AE events were detected and localized around one opening crack. Further active cracks, however, were not localizable. The reason for this is, and was discussed earlier, stress wave propagation is disrupted by open cracks in a specimen and therefore the source localization method fails.

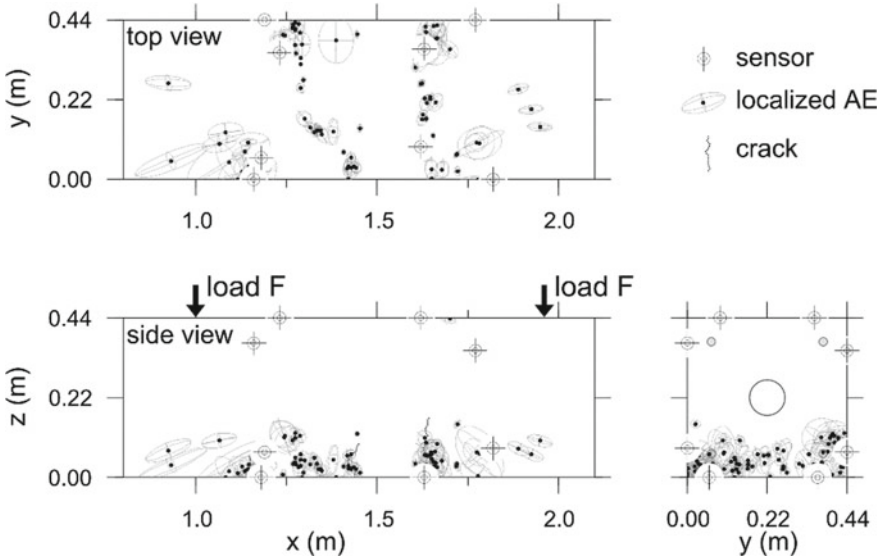

Fig. 26 Localization results during initial crack formation. Top view (top), elevation view (bottom, with cracks seen from the front side), and cross section (bottom right) of the loaded part of the test beam

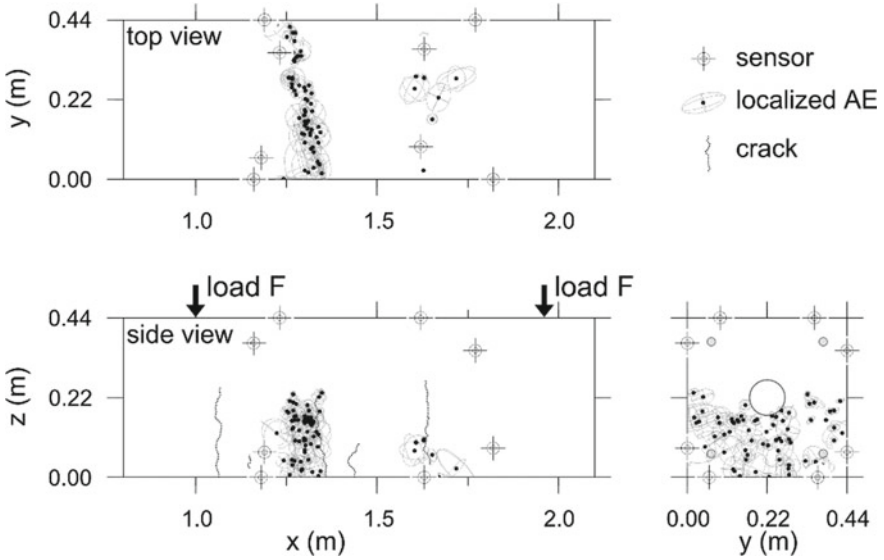

Fig. 27 Localization results during crack growing. Top view (top), elevation view (bottom, with cracks seen from the front side), and cross section (bottom right) of the loaded part of the test beam

In the example given above it becomes apparent that only a subset of all AE could be detected and even be localized with acceptable accuracy. Results thus only represent a portion of the actual fracture processes. The localization capability decreases with increasing damage (i.e. cracking) of the test specimen, especially when cracking of the material occurs in some regions and elastic waves are scattered and reflected.

4.3 Measures to Ensure High Localization Accuracy

The localization accuracy is influenced by various factors. In Table 1, some measures to ensure high localization accuracy are listed and discussed.

5 Further Methods

The methods described in this section were so far only partly applied to AEs. Since some of them are related to the approaches described in the preceding sections, they should be highly applicable to the AE localization problem. Numerous applications of these slightly more advanced methods, which e.g. consider clusters of sources rather than individual sources, exist in seismology. Further approaches developed or adapted for the AE localization problem presented in this section use e.g. neural networks or direct algebraic methods from GPS technology to localize AE sources. However, all methods presented in this chapter have in common that the travel time information from source to receiver is used.

5.1 Relative Localization Methods

If lateral velocity variations, which are common in the earth's structure, are present within a test region, and lead to uncertainties in the measured travel times at distant stations, the application of a relative localization procedure can improve the localization accuracy. This procedure can be only applied to a local region, i.e. the inter-event distances must be small compared to the event-receiver distance. The events within this region are relocalized relative to one particularly well-localized event, called master event. It is assumed that these velocity variations have nearly the same effect on all events from the local region (Shearer 1999). Equation 7 can be rewritten as:

$$r_i^{rel} = t_i^0 - t_i^{master} \tag{25}$$

The master event is used as the first guess location and Eq. 19 can be easily rewritten as:

Table 1 Factors influencing the accuracy of AE results

Measure		Effect
Data acquisition	Use of adequate number of sensors	Using more sensors than necessary, the localization algorithm is over determined and the variance, σ can be calculated as a measure of accuracy of the result. In general, the localization accuracy increases with increasing number of sensors employed Due to the limited reach of AE sensors, high numbers of sensors are needed to cover real-life structures. If only a certain number of sensors is available, concentration on areas of particular interest is recommended
	Appropriate sensor arrangement	Uniform azimuthal coverage of AE sources ensures that errors in arrival time determination do not lead to high uncertainties in the AE localization Limitations to the optimal sensor arrangement are posed by the specimen geometry
	Minimization of noise	The minimization of noise improves the SNR and therefore also the accuracy of the arrival time determination. This is achieved by using high-quality data acquisition components, proper shielding of cabling and electronics, and appropriate sensor coupling
Material model and localization approach	Determination of the wave speed, v in advance	Determining the wave speed, v in advance can be done without much effort, e.g. by performing PLBs at known locations. Applying the iterative localization method with a wrong v leads to systematic mislocalizations that might not manifest in high values of σ

(continued)

Table 1 (continued)

Measure		Effect
	Considering inhomogeneous material properties	By excluding sensors beyond known inhomogenities such as cracks, the accuracy of the localization result can be improved. The sensors to be excluded can be determined by evaluating station residuals, i.e. differences between calculated and measured arrival times after the source location has been estimated. The sensors with the largest station residuals are the ones that are excluded This method requires an iterative procedure and the use of a greater number of sensors. Results can be significantly improved when source localization techniques that consider heterogeneous material models are used
	Use of additional wave modes (other than P-waves)	For surface-near sources or planar localization, the use of surface waves, which are not as much attenuated as P-waves, increases the reach of the sensors. Using P- and S-waves, the accuracy of 3-D localizations can be improved The onsets of surface- and S-waves are generally difficult to detect in the recorded signals because they are hidden in the coda of the P-wave
Arrival time determination	Appropriate choice of threshold value	If the arrival time is determined using a fixed threshold exceedance criterion, the choice of the threshold value is crucial to the accuracy of the result For AE signals with a large variation of signal amplitudes, this method is not appropriate
	Use of sophisticated methods for arrival time determination	The use of sophisticated methods such as the AIC Picker (see Sect. 2.1) leads to a higher localization accuracy, in particular for signals that have a wide range of SNR

(continued)

Table 1 (continued)

Measure		Effect
	Manual arrival time determination	For AE signals with a low SNR, a manual determination is necessary to obtain reasonable localization results. For AE signals with a high SNR, the localization accuracy can be increased significantly The time needed for manual arrival time determination increases exponentially and can only be justified if few AE events have to be localized accurately for further analysis

$$\mathbf{r}^{rel} = \mathbf{G} \cdot \Delta\mathbf{x} \tag{26}$$

The correction vector, $\Delta\mathbf{x}$ must still be relatively small so that the linearization of the problem is valid. Since the principle of the relative localization procedure does not differ from the iterative one, the relative localization of AEs should also be possible. Further information about relative localization methods can be found in Deichmann and Garcia-Fernandez (1992), Mendecki (1997) or Shearer (1999).

5.2 Joint Hypocenter Determination

The relative localization method and joint hypocenter determination are both efficient ways to account for lateral velocity variations. However, in contrast to the relative localization method, the joint hypocenter determination method locates a group of events simultaneously to obtain a common set of sensor corrections. The following short overview of the method is referenced to the detailed outline of Pujol (2000).

The only difference between the single-event localization described in Sect. 3.4 and the joint hypocenter determination is that a correction term $\Delta\boldsymbol{s}$ for each sensor is added.

The system of $i = 1, \ldots, n$ sensors and $j = 1, \ldots, m$ events has to be solved simultaneously. Therefore, Eq. 19 can be rewritten as:

$$r_j = G_j \cdot \Delta x_j + \Delta s \tag{27}$$

The system of linear equations for joint hypocenter determination (Eq. 25) can be very large if many sensors and a large number of events are used. However, Pujol (2000) describes several methods in detail for an efficient solution of this problem.

Certain restrictions have also to be considered before a joint hypocenter determination can be applied. If the events are clustered very tightly, the solution will be

affected by intrinsic numerical errors (Pujol 2000). The joint hypocenter determination is used when unmodeled velocity variations are to be considered by determining station corrections. However, if the joint hypocenter should improve single event localization, the velocity variations need to be restricted to the portions of the raypath close to the sensor. Therefore, for improved results to be obtained, each station correction has to approximately represent the same travel time anomaly.

5.3 ΔT Source Localization

The **Δ**T source localization method (Baxter et al. 2007) was developed for the localization of AEs in a predefined area of interest. It was developed for plate-like structures. Therefore, the idea behind this approach is somehow related to the ideas of the relative localization and grid search methods with the possibility of considering non-linear material effects.

The application of the **Δ**T source localization method requires the generation of a grid on the surface of the component. With the help of artificially generated AEs, e.g. Hsu-Nielsen PLB sources, the time of arrival for each sensor is determined at the nodes of the grid. Then, for each sensor pair from each artificial source, the difference in time of arrival named "**Δ**T" is calculated. This leads to an interpolated **Δ**T map based on an average (5 events minimum) source difference for each node point. With the help of interpolation methods, the grid density can be increased. For localizing an AE event, ΔT is calculated for each sensor pair. Mapping these differences in time of arrival, while the time of arrival is determined by a threshold or a more advanced criterion, possible source locations are displayed. This leads to a convergence point representing the source of the AE. With increasing number of sensor pairs considered, the accuracy of the location is increased. A minimum of three sensors is required. The localization error is given as one grid square.

Similar to the approach from Baxter et al. (2007), the input data for the artificial neural network (ANN) localization approach of Kalafat and Sause (2015) is also based on the time of arrival differences, **Δ**T. In their study, a grid was applied to the specimen under investigation, which represents the locations of artificial AE sources of different frequency content. The resulting **Δ**T values were used to train the ANN. ANNs are a further tool that can be used for the localization of AE sources. Kalafat and Sause (2015) developed this approach especially for acoustic anisotropic and inhomogeneous fiber-reinforced materials.

A thorough discussion of the localization accuracy of this approach can be found in Kalafat and Sause (2015).

More recently, Al-Jumaili et al. (2016) present an efficient automatic iterative **Δ**T mapping technique using unsupervised clustering capable of locating AE sources in complex structures. They demonstrate that the accuracy is better than traditional time-of-arrival approach, as well as previous **Δ**T techniques.

5.4 Direct Algebraic Solvers

Direct algebraic solvers are common for global positioning systems (GPS) and are also based on a linearization of the localization approach. For the 3-D case, the point of intersection of hyperboloids is determined assuming a constant velocity. The application to AE source localization described in Kurz (2015) is based on the GPS approach developed by Bancroft (1985), which allows to solve the overdetermined case and calculate localization accuracies.

The basic equations for applying direct algebraic solvers are given in Eq. 28, which describes the transform of Eq. 17 into a form of so-called pseudo ranges, p_i and represents the hyperbolic surface of the position.

$$p_i = \sqrt{(x - x_i)^2 + (y - y_i)^2 (z - z_i)^2} + v \cdot t_0 \tag{28}$$

Equation 17 can be rearranged to the form shown in Eq. 29 describing the time-space continuum of the Minkowski space. Using mathematical matrix operations as described in Bancroft (1985) or Kurz (2015), the source point-location is obtained by ultimately solving a quadratic equation, i.e. two solutions exist containing the source coordinates and the pseudo-source time. The travel time residuals (difference between measured and calculated travel time) of the two solutions will differ significantly. Therefore, they are a measure for identifying the correct solution.

$$0 = (x - x_i)^2 + (y - y_i)^2 (z - z_i)^2 - v^2 \cdot (t_i - t_0)^2 \tag{29}$$

Direct algebraic solvers are fast since the applied mathematical operations are simple. Numerical instabilities cannot occur, however, criteria have to be defined to verify the plausibility of the results. One essential boundary condition regarding the application is that this approach requires the assumption of constant velocity and the onset times have to be determined. This has to be considered when applying this solver.

Besides of using the Bancroft solver for all onset times of all sensors for one event, the high speed of the numerical solver allows to divide the onsets of one event into subgroups. One such approach is described by Kurz (2015), where from 8 available onsets only 5 are taken for inversion. Building all five-event combinations leads to 56 localizations for one event. It is assumed and a requirement for the application of a refinement analysis that the resulting AE locations are clustering and condensing towards the correct location, i.e. incorrectly determined onsets can be figured out by statistical means. Here the median of the received localization coordinates (each axis separately) is determined and the difference between median and each event is calculated. This defines the extension of the event cluster and the source point is assumed as the center of mass of the resulting cluster.

5.5 Advanced Nonlinear Methods

Besides the iterative localization method, which is based on a linearization of the problem, and still one of the most frequently used methods, several nonlinear approaches exist for 3-D localization. Subsequently, three methods are summarized. The referenced papers contain further information about nonlinear source localization methods.

One approach to the nonlinear localization problem is the differential evolution algorithm by Ružek and Kvasnička (2001). The differential evolution algorithm is structured like a genetic algorithm and works efficiently and reliably. It is a robust global optimizer that does not use the linearized form of the problem, but minimizes Eq. 5 using a nonlinear approach.

As described in Sect. 5.1, a number of relative localization methods have been proposed in recent years. These methods apply to clusters of events and aim to reduce the hypocentral scatter of an event *cloud*. A popular method known as the *double-difference* method and developed by Waldhauser and Ellsworth (2000), considers both the P- and S-wave differential travel times, derived from cross-spectral methods, with travel time differences calculated for pairs of events. The method simultaneously determines inter-event distances between clusters of correlated events while determining the relative locations of other clusters and uncorrelated events. The *double-difference* earthquake localization algorithm allows the simultaneous relocalization of large numbers of events over large distances without the need of station corrections (see also joint hypocenter determination).

The residuals between the observed and calculated travel times between the two events, i and j recorded at site k, is defined by Waldhauser and Ellsworth (2000) as the *double-difference* and can be expressed as:

$$r_{ijk} = \left(t_{ik} - t_{jk}\right)^{obs} - \left(t_{ik} - t_{jk}\right)^{th} \tag{30}$$

Waldhauser and Ellsworth (2000) use a two-step iterative solution procedure, where a priori weights describing data quality are first applied to the arrival times. Once a stable solution is obtained, the data are reweighted by multiplying the a priori quality weights with values that depend on the misfit of the data from the previous iteration and on the offset between events (to downweight event pairs with large inter-event differences).

The double-difference method has been further developed by Spottiswoode and Linzer (2005). This method is referred to as the *hybrid* method because it is a combination of the double difference method and absolute (single event) methods, and is similar to the approach taken by Andersen (now Linzer) (2001) for moment tensor inversions (MTI). The *hybrid* method has evolved from the approach used by Spottiswoode and Milev (1998), who only considered groups of similar events.

One important enhancement is that events with additional constraints on their locations, such as explosions produced when developing a tunnel underground, are used to constrain the *hybrid* localizations. Another enhancement is that the median of

the distribution of residuals is used to weight the data. Experience gained by Andersen (2001) suggests that the use of median corrections is both more stable and more accurate even while the localization of individual events is based on weighted least-squares minimization. Additionally, the data recorded from closer sensors is given a greater weight, when absolute locations are computed using classical methods, to reduce errors caused by velocity errors from long ray paths.

For events i and j recorded at site k, Spottiswoode and Linzer (2005) define the residual as:

$$\begin{aligned}\left(r_{ijk}\right)^2 = & w^{ABS}\left[t_{ik}^{obs} - t_{ik}^{th}\right]^2 \\ & + w^{2D}\left[\left(t_{ik}^{obs} - t_{ik}^{th}\right) - median\left(t_{ik}^{obs} - t_{jk}^{th}\right)\right]^2 \\ & + \sum_2 w^{LINE}\left[d_i / v_k\right]^2 \end{aligned} \tag{31}$$

where d_i is the distance of event i from either of two planes through a known line of events (in an underground mining context, such a line could be the line of explosions produced when mining a tunnel), and v_k is the velocity assumed for the wave phase along the ray path. Equation 31 uses a reference *line* of events because this information was available. This formulation could be extended to include reference *points*, rather than lines. Although Eq. 31 may appear complicated, it is of a similar form to Eq. 30 if the travel times are regrouped as:

$$r_{ijk} = \left(t_{ik}^{obs} - t_{jk}^{th}\right) - \left(t_{jk}^{obs} - t_{jk}^{th}\right) \tag{32}$$

The first term in Eq. 31 is the absolute location component; the second term has the form of the double difference described by Eq. 30, and the last term represents the distance from two planes (oriented vertically and horizontally) that describe the reference line of events. The procedure is iterative and the weighting factors, (w^{ABS}, w^{2D}, w^{LINE}) control the influence of each term on the system of equations and are recalculated for each iteration. The arrival time differences between all pairs of events are used to obtain hybrid locations by minimizing the weighted sum of squares of all arrival-time differences. Minimization is done using the standard Gauss-Newton method (Press et al. 1990).

The hybrid localization procedure is being used successfully on data recorded in deep level mines in South Africa. A number of case studies are presented in Cichowicz et al. (2005).

5.6 *Probabilistic Methods*

Another alternative to standard iterative linearized localization methods is the probabilistic inversion approach of Tarantola and Valette (1982). In recent years, software

packages have become available that combine efficient, nonlinear, global search algorithms (e.g. *NonLinLoc*, Lomax et al. 2000). This method gained in importance for the precise localization of earthquake hypocenters (Husen et al. 2003) and can be adapted to the needs of AE localization with little modifications (Schechinger 2005). Results are more accurate and reliable compared to that of linearized localization methods and show more stability when linearized methods fail for events recorded outside of a sensor network. The nonlinear localization method can be easily applied with high-contrast 3-D-varying velocity models, because localization algorithms need no calculation of partial derivatives.

While standard linearized localization methods produce a single point solution and uncertainty estimates (Schechinger and Vogel 2006), the result of the nonlinear method is a probability density function (PDF) over the unknown source location coordinates. The optimal location is taken as the maximum likelihood point of the PDF. The PDF explicitly accounts for a priori known data errors, which are assumed to be Gaussian.

The model of the test specimen is discretized by a 3-D grid. For all grid nodes, travel times of the first arrivals to each sensor position have to be available. In *NonLinLoc*, a finite-difference scheme is used to calculate the travel time s for the given velocity model (Podvin and Lecomte 1991), but in principle, any method can be used. Different approaches are used for estimating the PDF. A systematic grid search algorithm over nested grids can be very time consuming but provides exhaustive coverage of the search region. The faster stochastic Metropolis-Gibbs sampling approach or the Oct-Tree Importance sampling algorithms are more practical for routine analysis (Lomax et al. 2000).

Solutions for two sample AE events, *E1* and *E2*, are shown in Fig. 28. They were recorded in a loading test of a reinforced concrete beam described in Sect. 4.2. The

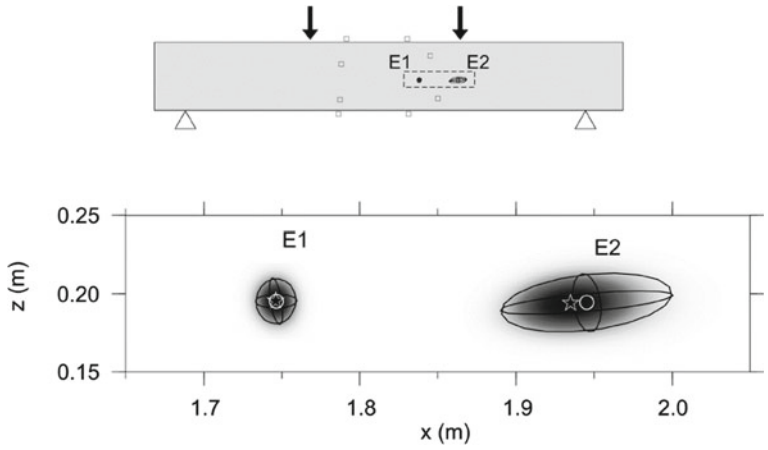

Fig. 28 Nonlinear localization results (using *NonLinLoc*) compared to linearized localization results. The 68% error ellipsoid estimated by the standard linearized localization method is plotted. See Fig. 25 for the experimental setup

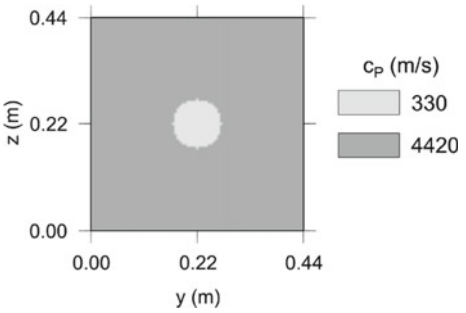

Fig. 29 Cross section of the 3-D velocity model with an air-filled void representing the ungrouted duct in the length axis of a concrete beam

results of the nonlinear localization (confidence volumes and maximum likelihood source coordinates, indicated by gray scales and white stars) are compared to the point source solution (white circles). The 68% error ellipsoids estimated by the standard linearized localization method is also plotted. In both cases, a constant propagation velocity was assumed. For the well observed Event *E1*, the two solutions are almost identical. Event *E2* occurred at the edge of the sensor network and therefore has a greater localization error. There are slight deviations between the error ellipsoid and the shape of the PDF, because the nonlinear relationship between source coordinates and travel times is taken into account. For this reason, the PDF can have a more irregular shape in the case of a 3-D velocity model.

The nonlinear localization method was further tested using a 3D velocity model on some events close to an ungrouted duct in the length axis of the concrete beam. Figure 29 shows the cross section of the model with an air-filled cylindrical void, along its length axis, that disturbs the direct wave propagation and hence the travel times.

The AE locations obtained with the linearized method for a homogeneous model of plain concrete differ from the results of the nonlinear localization with the 3-D model (Fig. 30). Ongoing work is investigating in detail how AE localization results are improved by the nonlinear approach. Possibilities for applications would be structures with large-scale inhomogeneities like hollow-cores.

A Bayesian probabilistic methodology developed specifically for AE localizations in concrete is presented in Schumacher et al. (2012) and Schumacher and Straub (2011). The authors developed a Bayesian framework using Monte Carlo Markov Chain (MCMC) simulation where the model parameters are represented by probability density functions (PDF). The premise of a Bayesian network approach is that these PDFs can be updated once events are observed that provide new information about them. Also, it is straight forward to include additional data and relationships to improve the prediction of future events. The authors used the open source program *WinBUGS*, a statistical software for Bayesian analysis using MCMC methods, for their localization methodology (Lunn et al. 2000). Before source localization can be performed using a predictive model, model parameters have to be estimated based on an inference model.

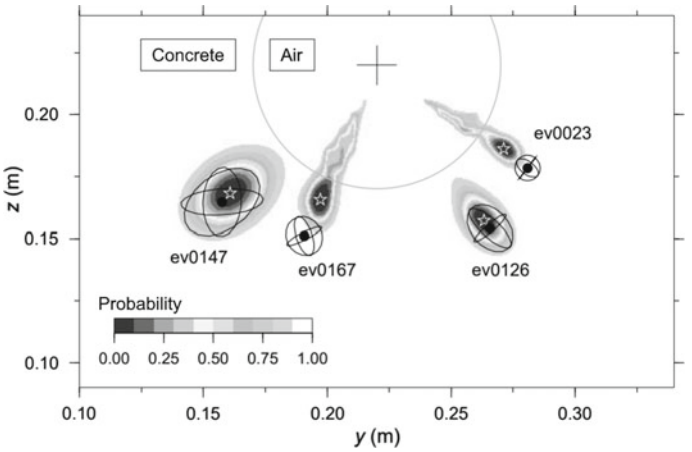

Fig. 30 Nonlinear localization results considering an air-filled duct (confidence levels in gray scales and maximum likelihood solution as stars) compared to linearized results for a plain concrete model (black circles as point source with error ellipsoid). Figure adapted from Schechinger (2005)

The equation to calculate the arrival time, t_a at sensor k can be expressed as follows (equivalent to Eq. 6):

$$t_{a[i,j,k]} = t_{0[i,j]} + s_{p[i,k]} d_{[i,k]} + \varepsilon_{[i,j,k]} \tag{33}$$

where t_0 is the unknown event time, s_p is wave slowness (inverse of wave speed, c_p, assumed constant), d is the wave travel distance between the source and sensor k (assumed as straight), and ε is an error term modeled as a Gaussian variable with zero mean and precision, τ (inverse of standard deviation, σ). Indices, i, j, and k denote source locations, events at the same source location (used for PLBs), and sensors, respectively, imposing a distinct hierarchy in the model. The wave travel distance is calculated as:

$$d_{[k]} = \sqrt{(x_{[k]} - x_0)^2 + (y_{[k]} - y_0)^2 + (z_{[k]} - z_0)^2} \tag{34}$$

where $x_{[k]}$, $y_{[k]}$, and $z_{[k]}$ are the coordinates of sensor, k and x_0, y_0, and z_0 are the unknown source coordinates.

Alternatively, Eq. 33 can be expressed as a probabilistic model, as follows (Schumacher and Straub 2011):

$$T_{a[i,j,k]} \sim \mathrm{N}\left(t_{0[i,j]} + s_{p[i,k]} d_{[i,k]},\ \tau_{\varepsilon[i,j,k]}\left(A_{[i,j,k]},\ \alpha\right)\right) \tag{35}$$

where A is the signal amplitude and α is a global parameter that relates the precision of the errors in the observed arrival times τ with the signal amplitude. Following examination of arrival time picking errors, Δt and shifted signal amplitude, A-A_{min},

it was observed that the variance of the picking error decreases with increasing signal amplitude. Hence, the following relationship was employed in the model:

$$\tau_{\varepsilon[i,j,k]} = A_{[i,j,k]}\alpha \tag{36}$$

The graphical representations of the inference model and the prediction model are provided in Figs. 31 and 32. Round and rectangular nodes represent random variables and constants, respectively. In order to estimate the model parameters (round nodes), prior distributions have to be defined. The authors used weakly informative priors, corresponding to normal distributions with low precisions. Once the model parameters are estimated and bounds (e.g. to keep predictions within the specimen's geometric boundaries) are defined, localizations can be performed on newly available data, i.e. arrival times.

Results can be visualized in form of a point cloud colored according to density and the optimal point solution can be computed using a mean-shift algorithm, representing the highest density point of the cloud. A sample localization result from a PLB test performed on a reinforced concrete specimen with overall dimensions, 0.61 $\times$ 0.61 $\times$ 1.83 m is shown in Fig. 33.

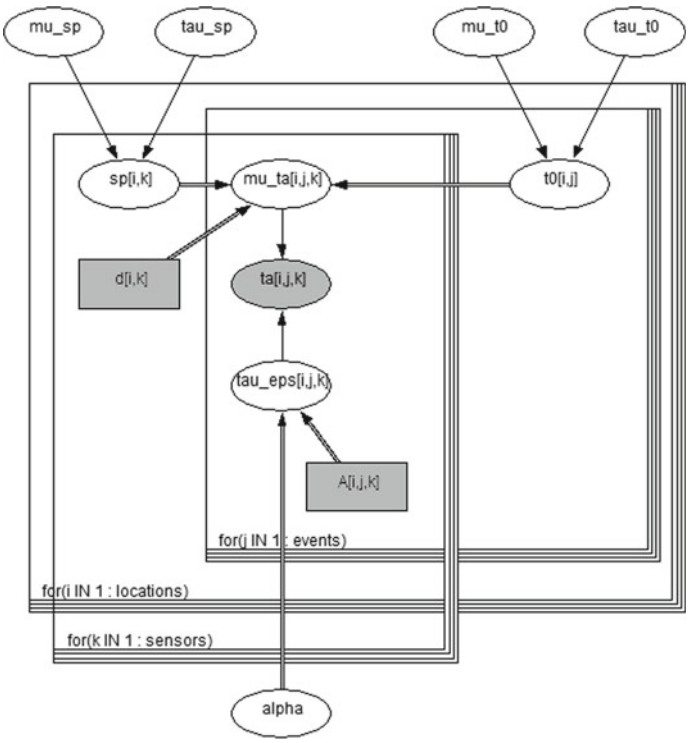

Fig. 31 Graphical representation of the inference model

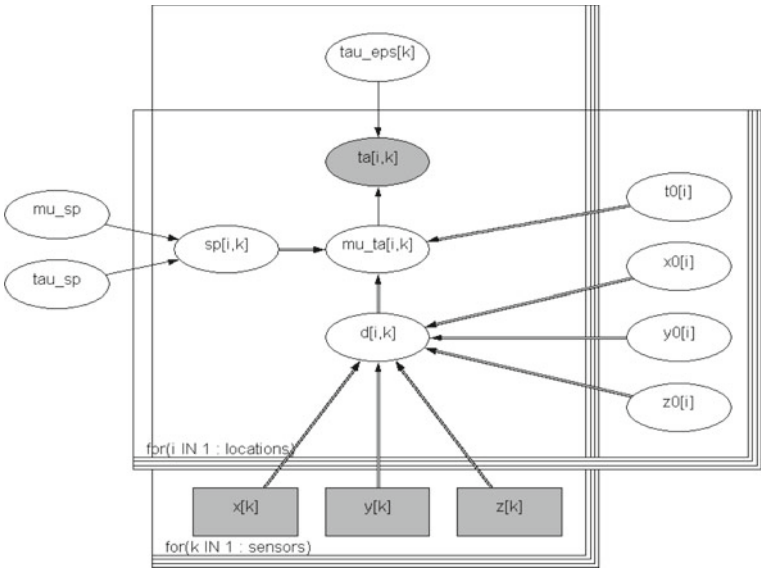

Fig. 32 Graphical representation of the prediction model

A comparison of 22 PLB applied on the *x*-*z* front face of the specimen showed that the Bayesian probabilistic source localization outperformed the traditional iterative technique significantly. An advantage is that additional information and relationships can be readily in included in the model to further improve the accuracy. Finally, spatial as well as temporal source location parameters are available in probabilistic form, providing an improved measure of uncertainty compared to the error ellipsoid.

A limitation of this methodology is that it assumes a constant wave velocity and straight wave travel paths.

A robust hypocenter localization code called BEMIS (Bayesian Estimation of Mine Induced Seismicity—see Martinsson 2013) is currently being tested at Kiruna mine in Sweden. Kiruna mine has one of the world's largest in-mine seismic networks consisting of >300 triaxial and uniaxial geophones and records >10,000 seismic events every day. The mining-induced stress changes are relatively slow and an average of 2700 $M_W \geq 0$ seismic events are recorded every year, with the largest event recorded on May 18, 2020 having a moment magnitude, Mw 4.3 (Dahner-Lindkvist and Dineva 2020).

BEMIS is designed to increase the accuracy and precision of the hypocenters that have poor, inconsistent, and insufficient phase arrival times by introducing heavy-tailed distributions and an informative prior distribution of the seismicity (Martinsson 2013). Arrival time outliers can be caused by a variety of influences, for example, velocity changes due to the fracture zone, weak emergent arrivals, etc. Previous studies have shown that travel time residual distributions often do not follow normal distributions with respect to the occurrence of extreme values and outliers, and

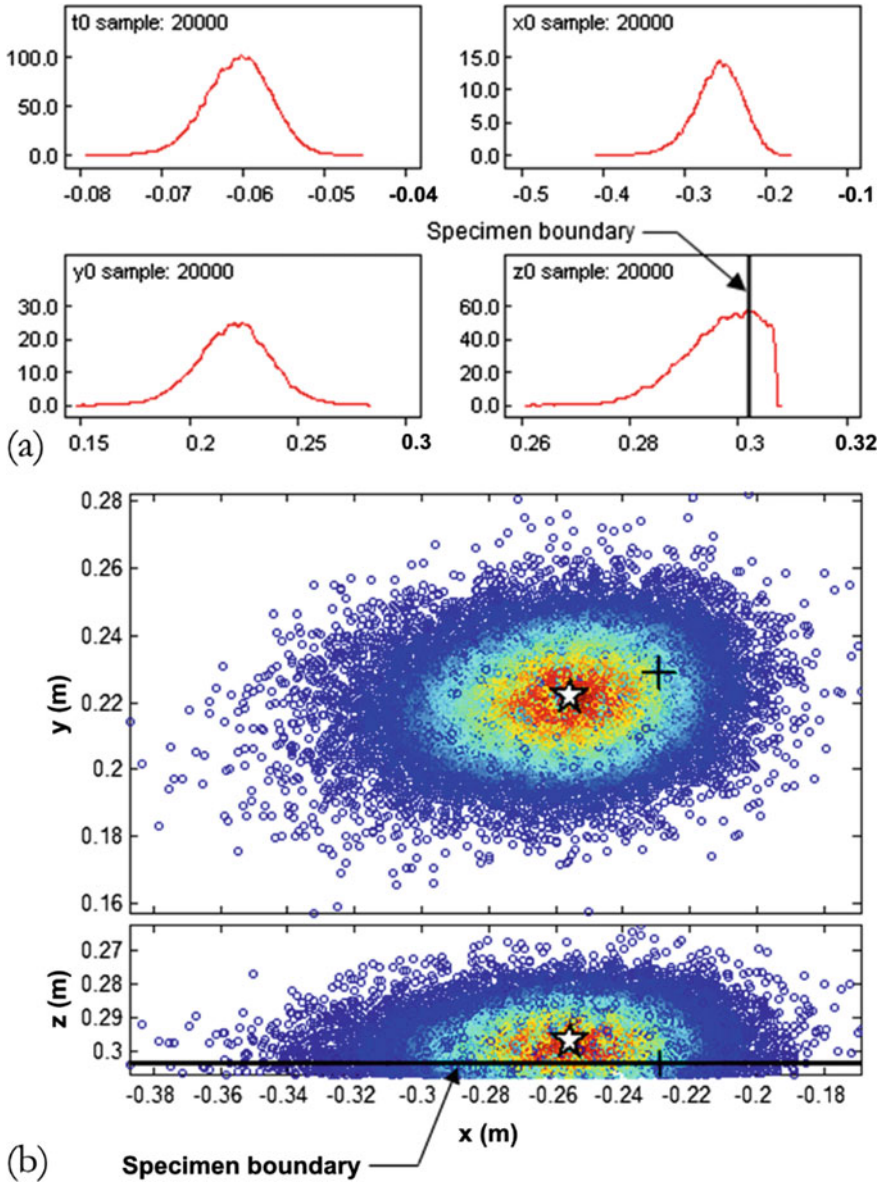

Fig. 33 Sample localization result: **a** Kernel density estimates for predicted source location parameters and **b** visualization using point density cloud with optimal solution shown as white pentagram. Figure adapted from Schumacher and Straub (2011)

suggest distributions with heavier tails (e.g. Buland 1986; Grand 1990) and multimodal (Bondár et al. 2004) characteristics. A number of deterministic approaches have been considered applying different norms of the equation error (e.g. Prugger and Gendzwill 1988; Blair 1993; Mendecki 1993).

Martinsson (2013) also applied a Gaussian Mixture Model (GMM) to increase the robustness against poor, inconsistent, or insufficient arrivals. The GMM uses a hypocenter prior distribution to describe the seismically active areas, where the parameters are estimated based on previously localized events in the region. The prior distribution is truncated to constrain the localization solution to valid geometries, for example below the ground surface, excluding known mined out voids and fracture zones.

To reduce the sensitivity to outliers, Martinsson evaluated different heavy-tailed distributions to model the likelihood distribution of the arrivals given the hypocenter and the origin times. The multivariate *t*-distribution was shown to produce the overall best performance, where the tail-mass adapts to the observed data. Markov Chain Monte Carlo (MCMC) techniques were then applied to determine hypocenter and uncertainty region estimates.

Underground seismic networks have an advantage over AE tests in the laboratory because the velocity model can be continually updated using blasts from known locations. In laboratory tests, this could be mimicked by either periodically (a) performing PLBs on the specimen surface or (b) by transmitting pulses from each transducer in the network one-by-one.

The BEMIS processing chain is fully automated and the P- and S-wave arrival times with corresponding uncertainties are estimated from the seismograms using simple multivariate autoregressive (MAR) descriptions of the seismograms following Basseville and Nikiforov (1993). The MAR technique produces a 46% reduction in the average localization error when compared against the currently used deterministic localization technique based on manual estimation of the P- and S-wave arrival times.

5.7 Time Reversal Methods

Kocur (2012) developed an AE source localization method for application on structural concrete based on time reverse modeling (TRM). The central idea behind TRM is that if AE signals recorded from an event are reversed in time and reemitted into the test specimen, they should constructively interfere at their location of origin. The source location emerges as a region of concentrated energy. While the recorded signals can be either from physical experiments or numerical simulations, the time reversal part is always performed by numerical wave simulation. A detailed numerical model of the test specimen containing information on a finite grid regarding wave mode velocities and density is the basis for the wave simulation. Kocur first established the general methodology using numerically simulated signals that employed a realistic numerical concrete model. This model was developed by performing segmented X-ray tomography on a real concrete specimen (Kocur et al. 2010).

To prove that the approach works for localizing AE signals, Kocur tested a 0.12 × 0.12 × 1.70 m reinforced concrete beam to failure (Kocur et al. 2016). The specimen was equipped with eight AE transducers attached to the surface. To verify the AE source location maps, segmented X-ray tomography was performed throughout the test to establish detailed crack maps and to provide data for the material model required to apply the technique. The TRM localization maps were then overlaid with the crack maps for comparison.

The TRM approach opens exciting avenues not only for improved localization of events but under some circumstances it might even be possible to gain insight into the source mechanism of an event. Kocur showed this for the case of numerically simulated signals in his work where he was able to visualize the radiation pattern of different source mechanisms under simplified conditions (Kocur 2012). The challenges with TRM is that it relies, similar to Gollob's approach described in Sect. 3.2, on a detailed numerical model of the test specimen. Establishing an accurate 3D material model, which is unique for every structure, is not only time consuming but in many cases might not be possible. Additionally, the wave simulations are computationally expensive, requiring super computers to complete localizations in a reasonable time.

References

Abukamov I, Roeser A, Shapiro SA (2020) Arrival-time picking uncertainty: theoretical estimations and their application to microseismic data. Geophysics 85(4). https://doi.org/10.1190/geo2019-0589.1

Akaike H (1974) Markovian representation of stochastic processes and its application to the analysis of of autoregressive moving average processes. Ann Inst Stat Math 26:363–387

Aki K, Richards P (1980) Quantitative seismology theory and methods, vol 2. Freeman WH and Company, New York

Al-Jumaili SK, Pearson MR, Holford KM, Eaton MJ, Pullin R (2016) Acoustic emission source location in complex structures using full automatic delta T mapping technique. Mech Syst Signal Process 72–73:513–524. https://doi.org/10.1016/j.ymssp.2015.11.026

Allen R (1982) Automatic phase pickers: their present use and future prospects. Bull Seismol Soc Am 72:225–242

Andersen LM (2001) A relative moment tensor inversion technique applied to seismicity induced by mining. PhD Thesis, University of the Witwatersrand, Johannesburg

Andersen LM, Spottiswoode SM (2001) A hybrid relative moment tensor methodology. In: 5th international symposium on rockbursts and seismicity in mines, South African Institute of Mining and Metallurgy, pp 371–378

Baer M, Kradolfer U (1987) An automatic phase picker for local and teleseismic events. Bull Seismol Soc Am 77:1437–1445

Bancroft S (1985) An algebraic solution of the GPS equations. IEEE Trans Aerosp Electron Syst 21:56–59

Basseville M, Nikiforov IV (1993) Detection of abrupt changes—theory and applications. Prentice-Hall, Englewood Cliffs, NJ

Bath M (1979) Introduction to seismology, 2nd edn. Birkhäuser Verlag, Basel

Baxter MG, Pullin R, Holford KM, Evans SL (2007) Delta T source location for acoustic emission. Mech Syst Signal Process 21(3):1512–1520

Berthelot JM, Robert J (1987) Modelling concrete damage by acoustic emission. J Acoust Emiss 6:43–66
Blair DP (1993) A comparative study of seismic source location methods in underground mines. In: Proceedings of rockbursts and seismicity in mines, Rotterdam, The Netherlands, pp 321–325
Bondár I, Myres SC, Engdahl ER, Bergman EA (2004) Epicentre accuracy based on seismic network criteria. Geophys J Int 156:483–496
Bormann P (ed) (2002) New manual of seismological observatory practice, vol 1 & 2 GeoForschungsZentrum Potsdam
Brigham EO (1974) The fast fourier transform. Prentice Hall Inc., Englewood Cliffs USA
Buland R (1986) Uniform reduction error analysis. Bull Seismol Soc Am 66:173–187
Capon J (1969) High-resolution frequency-wavenumber spectrum analysis. Proc IEEE 57(8):1408–1418
Cichowicz A, Spottiswoode SM, Linzer LM, Drent D, Heyns PS, Handley MF (2005) Improved seismic locations and location techniques (SIMRAC Report SIM020304), Department of Minerals and Energy, South Africa www.simrac.co.za
Dai H, MacBeth C (1995) Automatic picking of seismic arrivals in local earthquake data using an artificial neural network. Geophys J Int 120:758–774
Dahner-Lindkvist C and Dineva S (2020) Small-scale variations in mining-induced stresses, monitored in a seismically active underground mine. In: Wesseloo J (ed) Underground mining technology 2020, Australian Centre for Geomechanics, Perth, ISBN 978-0-9876389-9-1
Deichmann N, Garcia-Fernandez M (1992) Rupture geometry from high-precision relative hypocenter locations of microearthquake clusters. Geophys J Int 110:501–517
Dijkstra EW (1959) A note on two problems in connexion with graphs. Numer Math 1:269–271. https://doi.org/10.1007/BF01386390
Dill-Langer G, Ringger T, Höfflin L, Aicher S (2002) Location of acoustic emission sources in timber loaded parallel to grain. In: 13th international symposium on nondestructive testing of wood, August 19–21, Berkeley, California
Dubuc B, Ebrahimkhanlou A, Salamone S (2018) Localization of multiple acoustic emission events occurring closely in time in thin-walled pipes using sparse reconstruction 29(11):2362–2373. https://doi.org/10.1177/1045389X18770857
Earle P, Shearer P (1994) Characterization of global seismograms using an automatic picking algorithm. Bull Seismol Soc Am 84(2):366–377
Finck F (2005) Untersuchung von Bruchprozessen in Beton mit Hilfe der Schallemissionsanalyse. PhD thesis, University of Stuttgart
Finck F, Manthei G (2004) On near-field effects in signal based acoustic emission analysis. Otto Graf J 15:121–134
Finck F, Yamanouchi M, Reinhardt HW, Grosse C (2003) Evaluation of mode-I failure of concrete in a splitting test using acoustic emission technique. Int J Fract 124:139–152
Flinn E (1965) Confidence regions and error determinations for seismic event location. Rev Geophys 3(1):157–185
Gollob S (2017) Source localization of acoustic emissions using multi-segment paths based on a heterogeneous velocity model in structural concrete. PhD dissertation ETH Zurich, https://doi.org/10.3929/ethz-a-010870031
Gollob S, Kocur GK, Schumacher T, Mhamdi L, Vogel T (2017) A novel multi-segment path analysis based on a heterogeneous velocity model for the localization of acoustic emission sources in complex propagation media. Ultrasonics 74(2):48–61. https://doi.org/10.1016/j.ultras.2016.09.024
Grand SP (1990) A possible station bias in travel time measurements reported to ISC. Geophys Res Lett 17:17–20
Grosse CU, Reinhardt HW (1999) Entwicklung eines Algorithmus zur automatischen Lokalisierung von Schallemissionen. Die Materialprüfung 41:342–347
Grosse CU (1996) Quantitative zerstörungsfreie Prüfung von Baustoffen mittels Schallemissionsanalyse und Ultraschall. PhD thesis, University of Stuttgart

Grosse CU (2005) Akustische Verfahren zur zerstörungsfreien Prüfung von Baustoffen und Bauteilen. Habilitation thesis, University of Stuttgart, 148 p
Grosse CU, Glaser SD, Krüger M (2006) Condition monitoring of concrete structures using wireless sensor networks and MEMS. In: Tomizuka M, Yun CB, Giurgiutiu V (eds) Proc SPIE, vol 6174, Smart structures and materials 2006: sensors and smart structures technologies for civil, mechanical, and aerospace systems, pp 407–418
Havskov J, Bormann P, Schweitzer J (2002) Chapter IS 11.1: earthquake location. In: Bormann P (ed), New manual of seismological observatory practice, vol 2. GeoForschungsZentrum Potsdam, p 28
Husen S, Kissling E, Deichmann N, Wiemer S, Giardini D, Baer M (2003) Probabilistic earthquake location in complex three-dimensional velocity models: Application to Switzerland. J Geophys Res 108(B2):2077. https://doi.org/10.1029/2002jb001778
Joswig M (2004) Nanoseismic monitoring—Part I: theory and first applications. Geophys J Int (submitted)
Joswig M (1990) Pattern recognition for earthquake detection. Bull Seismol Soc Am 80:170–186
Kalafat S, Sause MGR (2015) Acoustic emission source localization by artificial neural networks. Struct Health Monitor 14(6):633–647
Kapphahn G, Quade J, Steffens K (1993) SEA-Prüfung bei der insitu-Traglastermittlung von Stahl- und Spannbetonkonstruktionen. In: Jubiläungstagung 60 Jahre DGZfP, 17.–19. Mai 1993 in Garmisch-Partenkirchen, DGZfP Berlin
Kitagawa G, Akaike H (1978) A procedure for the modelling of non-stationary time series. Ann Inst Stat Math 30 (Part B):351–363
Kocur GK, Saenger EH, Grosse CU, Vogel T (2016) Time reverse modeling of acoustic emissions in a reinforced concrete beam. Ultrasonics 65:96–104
Kocur GK (2012) Time reverse modeling of acoustic emissions in structural concrete. ETH Zürich, doctoral thesis, ETH No. 20368
Kocur GK, Saenger EH, Vogel T (2010) Elastic wave propagation in a segmented X-ray computed tomography model of a concrete specimen. Constr Build Mater 24:2393–2400
Köppel S (2002) Schallemissionsanalyse zur Untersuchung von Stahlbetontragwerken, ETH Zürich, IBK Bericht 272, Zürich, p 174
Köppel S, Vogel T (2000) Schallemissionsmessungen bei Versuchen an Stahlbeton. ETH Zürich, IBK Bericht 259:164
Köppel S, Grosse C (2000) Advanced acoustic emission techniques for failure analysis in concrete. In: WCNDT proceedings 2000. Italian Society for Non-Destructive Testing and Monitoring Diagnostics
Kreyszig E (1993) Advanced engineering mathematics, 7th edn, John Wiley & Sons Inc
Kundu T (2014) Acoustic source localization. Ultrasonics 54:25–38
Kurz JH (2015) New approaches for automatic threedimensional source localization of acoustic emission—applications to concrete specimens. Ultrasonics 63:155–162
Kurz JH (2006) Verifikation von Bruchprozessen bei gleichzeitiger Automatisierung der Schallemissionsanalyse an Stahl- und Stahlfaserbeton. PhD thesis, University of Stuttgart
Kurz JH, Grosse CU, Reinhardt HW (2005) Strategies for reliable automatic onset time picking of acoustic emissions and of ultrasound signals in concrete. Ultrasonics 43(7):538–546
Labusz J, Chang H, Dowding C, Shah S (1988) Parametric study of AE location using only four sensors. Rock Mech Rock Eng 21:139–148
Leonard M (2000) Comparison of manual and automatic onset time picking. Bull Seismol Soc Am 90(6):1384–1390
Lomax A, Virieux J, Volant P, Berge-Thierry C (2000) Probabilistic earthquake location in 3D and layered models. In: Thurber C, Rabinowitz N (eds), Advances in seismic event location. Kluwer Academic Publishers, pp 101–134
Lunn DJ, Thomas A, Best N, Spiegelhalter D (2000) WinBUGS—a Bayesian modelling framework: concepts, structure, and extensibility. Stat Comput 10:325–337

Maeda N (1985) A method for reading and checking phase times in auto-processing system of seismic wave data. Zisin (= Jishin) 38:365–379
Martinsson J (2013) Robust Bayesian hypocentre and uncertainty region estimation: the effect of heavy-tailed distributions and prior information in cases with poor, inconsistent and insufficient arrival times. Geophys J Int 192:1156–1178
Mendecki AJ (ed) (1997) Seismic monitoring in mines, 1st edn. Chapman & Hall, London
Mendecki AJ (1993) Real time quantitative seismology in mines. In: Proceedings of rockbursts and seismicity in mines, Rotterdam, The Netherlands, pp 287–295
Mhamdi L (2015) Seismology-based approaches for the quantitative acoustic emission monitoring of concrete structures, PhD dissertation University of Delaware. http://udspace.udel.edu/handle/19716/17497
Mhamdi L, Schumacher T (2015) A comparison between time-of-arrival and novel phased array approaches to estimate acoustic emission source locations in a steel plate. J Nondestr Eval 34(4):38. https://doi.org/10.1007/s10921-015-0311-y
Moriya H, Manthei G, Mochizuki S, Asanuma H, Niitsuma H, Jones R, Eisenblätter J (2002) Collapsing method for delineation of structures inside AE cloud associated with compression test of salt rock specimen. In: The 16th International Acoustic Emission Symposium, November 12–15 2002, Tokushima, Japan
Ohtsu M (1998) Basics of acoustic emission and applications to concrete engineering. Mater Sci Res Int 4(3):131–140
Podvin P, Lecomte I (1991) Finite difference computation of traveltimes in very contrasted velocity models: a massively parallel approach and its associated tools. Geophys J Int 105:271–284
Press W, Teukolsky S, Vetterling W, Flannery B (1992) Numerical recipes in C. Cambridge University Press, New York, Sect. 15.6, pp 689–699
Press WH, Flannery BP, Teukolsky SA, Vetterling WT (1990) Numerical recipes: the art of scientific computing. Cambridge University Press, New York
Prugger AF, Gendzwill DJ (1988) Microearthquake location: a nonlinear approach that makes use of a simplex stepping procedure. Bull Seismol Soc Am 78:799–815
Pujol J (2000) Joint event location—the JHD technique and application to data from local seismic networks. In: Thurber C, Rabinowitz N (eds) Advances in seismic event location. Kluwer Academic Publishers, pp 163–204
Pujol J (2004) Earthquake location tutorial: graphical approach and approximate epicentral location techniques. Seismol Res Lett 75(1):63–74
Reinhardt HW, Grosse CU (1999) Zerstörungsfreie Prüfung von Aramidbewehrung. In: Teutsch M (ed), Festschrift zum 60. Geburtstag von Univ.-Prof. Dr.-Ing. Horst Falkner. vol 142. Institut für Baustoffe, Massivbau und Brandsschutz, pp 233–240
Rost S, Thomas C (2002) Array seismology: methods and applications. Rev Geophys 40(3):1008. https://doi.org/10.1029/2000rg000100
Ružek B, Kvasnička M (2001) Differential evaluation algorithm in the earthquake hypocenter location. Pure appl Geophys 158:667–693
Schechinger B, Vogel T (2006) Acoustic emission for monitoring a reinforced concrete beam subject to four-point-bending. Constr Build Mater 21(3):483–490
Schechinger B (2005) Schallemissionsanalyse zur Überwachung der Schädigung von Stahlbeton. PhD thesis, Eidgenössische Technische Hochschule Zürich
Schumacher T, Straub D, Higgins C (2012) Toward a probabilistic acoustic emission source location algorithm: a Bayesian approach. J Sound Vib 331(19):4233–4245. https://doi.org/10.1016/j.jsv.2012.04.028
Schumacher T, Straub D (2011) A Bayesian acoustic emission source location algorithm: extended model. Appl Stat Probab Civ Eng (Proceedings of ICASP11. Zurich, Switzerland. August 1–4, 2011):91–98. https://doi.org/10.1201/b11332-16
Sedlak P, Hirose Y, Enoki M (2013) Acoustic emission localization in thin multi-layer plates using first-arrival determination. Mech Syst Signal Process 36(2):636–649. https://doi.org/10.1016/j.ymssp.2012.11.008

Sellers E, Kataka M, Linzer L (2003) Source parameters of acoustic emission events and scaling with mining-induced seismicity. J Geophys Res 108(B9). https://doi.org/10.1029/2001jb000670
Sleeman R, van Eck T (1999) Robust automatic P-phase picking: an on-line implementation in the analysis of broadband seismogram recordings. Phys Earth Planet Inter 113:265–275
Spies T, Hesser I, Eisenblätter J (2004) Seismology on a small scale: acoustic emission measurements in rock mechanics. In: Schweitzer J (ed), Symposium in memoriam of Prof. Gerhard Müller, vol I/2004, Mitteilungen Sonderband, Deutsche Geophysikalische Gesellschaft, 72–76
Spottiswoode SM, Linzer LM (2005) A hybrid location methodology. J S Afr Inst Min Metall 105:417–425
Spottiswoode SM, Milev A (1998) The use of waveform similarity to define planes of mining-induced seismic events. Tectonophysics 289:51–60
Schweitzer J, Fyen J, Mykkeltveit S, Kvaerna T (2002) Chapter 9: Seismic arrays. In: Bormann P (ed), New manual of seismological observatory practice, vol 1. GeoForschungsZentrum Potsdam, p 51
Shearer P (1999) Introduction to seismology. Cambridge University Press
Smart E, Flin E (1971) Fast frequency-wavenumber analysis and fisher signal detection in real-time infrasonic array data processing. Geophys J Roy Astron Soc 26:279–284
Tarantola A (2005) Inverse problem theory and methods for model parameter estimation. https://doi.org/10.1137/1.9780898717921
Tarantola A, Valette B (1982) Inverse problems = quest for information. J Geophys 50:159–170
Thurber C, Engdahl E (2000) Advances in global seismic event location. In: Thurber C, Rabinowitz N (eds), Advances in seismic event location. Kluwer Academic Publishers, pp 3–22
Trnkoczy A (2002) Understanding and paramter settings of STA/LTA trigger algorithm. In: Bormann P (ed) IASPEI New manual of seismological observatory practice, vol 2, GeoForschungsZentrum Potsdam, Ch. IS 8.1, pp 1–19
Waldhauser F, Ellsworth W (2000) A double-difference earthquake location algorithm: method and application to the Northern Hayward Fault, California. Bull Seismol Soc Am 90(6):1353–1368
Zang A, Wagner C, Stanchits S, Dresen G, Andresen R, Haidekker M (1998) Source analysis of acoustic emissions in Aue granite cores under symmetric and asymmetric compressive loads. Geophys J Int 135:1113–1130
Zhang H, Thurber C, Rowe C (2003) Automatic P-wave arrival detection and picking with multiscale wavelet analysis for single-component recordings. Bull Seismol Soc Am 93(5):1904–1912
Zwicky D, Vogel T (2000) Bruchversuche an ausgebauten Brückenträgern aus Spannbeton; ETH Zürich, IBK Bericht 258, Zürich, p 167